



PerTPV – Perovskite thin film photovoltaics

Grant agreement 763977

## Deliverable 1.7

### Report on final new materials

WP1

**Lead beneficiary:** KTU

**Authors:** Tadas Malinauskas, Michele Sessolo, Henk Bolink, Henry Snaith

**Delivery date:** 31/03/2021

**Confidentiality level:** Public



*The PerTPV project has received funding from the European Union's Horizon 2020 research and innovation programme under grant agreement No 763977.*

# Revision History

Author Name, Partner short name	Description	Date
Tadas Malinauskas, KTU	Draft deliverable	18/03/2021
Henry Snaith	Revision 1	29/03/2021
	Final version	31/03/2021

## Contents

REVISION HISTORY .....	2
CONTENTS .....	2
INTRODUCTION.....	3
<b>1. DEVELOPMENT OF PEROVSKITE ABSORBERS .....</b>	<b>3</b>
1.1 VAPOUR DEPOSITED WIDE BANDGAP PEROVSKITE ABSORBERS (UEVG) .....	3
1.2 VAPOUR DEPOSITED LOW BAND GAP Pb:SN PEROVSKITE ABSORBERS (UEVG) .....	5
1.3 SOLUTION PROCESSED NARROW BAND GAP ABSORBER (UOXF).....	9
1.4. SOLUTION PROCESSED WIDE BAND GAP ABSORBER (UOXF).....	11
<b>2. DEVELOPMENT OF N-TYPE MATERIALS.....</b>	<b>13</b>
2.1. ALTERNATIVE NON-FULLERENE ETMS FOR VACUUM DEPOSITED DEVICES (UEVG) .....	13
2.2. ALTERNATIVE NAPHTHALENETETRACARBOXYLIC DIIMIDE ETMS (KTU).....	16
<b>3. DEVELOPMENT OF P-TYPE MATERIALS .....</b>	<b>19</b>
3.1. SHALLOW HOMO HOLE TRANSPORTING MATERIALS (KTU) .....	19
3.1.1 Spirobifluorene and fluorene-based derivatives .....	19
3.1.2 Carbazole-based enamines .....	22
3.2. DEEP HOMO HOLE TRANSPORTING MATERIALS (KTU) .....	26
3.2.1 Spirofluorene-based enamines.....	26
3.2.3 Tröger's base derivative containing larger diphenylbenzidine units.....	28
3.3. HOLE TRANSPORTING MATERIALS CAPABLE OF FORMING SELF-ASSEMBLED MONOLAYERS (KTU) .....	30
<b>4. CONCLUSIONS .....</b>	<b>30</b>
4.1. PEROVSKITE ABSORBERS .....	30
4.1.1 Solution processed wide bandgap perovskite absorbers .....	31
4.1.2 Solution processed narrow bandgap perovskite absorbers .....	31
4.1.3 Vacuum deposited wide bandgap perovskite absorbers .....	31
4.1.4 Vacuum deposited narrow bandgap perovskite absorbers .....	31
4.2. CHARGE TRANSPORTING MATERIALS.....	31
4.2.1 Electron transporting materials .....	31
4.2.2 Hole transporting materials.....	32



The PerTPV project has received funding from the European Union's Horizon 2020 research and innovation programme under grant agreement No 763977.

# Introduction

One of the important objectives of the project is development of tandem devices containing compatible wide and narrow bandgap perovskite absorbers. The aim for the low bandgap perovskite is 1.2 to 1.3 eV, the target bandgap for the wide bandgap perovskite is 1.7 to 1.8 eV as identified in D1.1.

The main objective of WP1 is to deliver an ideal and stable set of materials for single junction and tandem all-perovskite solar cells. This includes the absorber materials as well as the charge selective layers.

Obviously, for these perovskite tandem devices to function effectively, development of efficient charge extracting materials, matching the energy levels of the wide and low bandgap perovskite absorbers, is an important task. Therefore, as a step towards the development of tandem devices, we have investigated several different groups of charge transporting materials with suitable energy levels to be used further in the project.

PERTPV is aiming to prepare both single and multiple junction perovskite solar cells, using processes that are compatible with industrial methods for large volume manufacturing. In particular, solution-based slot die-coating and printing methods in parallel to vacuum sublimation and chemical vapour deposition methods for the formation of the perovskite absorber layers and the charge transport and recombination layers. Therefore, development of aforementioned charge transporting materials has to be conducted in two directions: solution processable and thermally sublimable compounds.

## 1. Development of perovskite absorbers

### 1.1 Vapour deposited wide bandgap perovskite absorbers (UVEG)

We have developed a 4-sources vacuum deposition process to prepare wide-bandgap perovskites of the type  $\text{FA}_{1-n}\text{Cs}_n\text{Pb}(\text{I}_{1-x}\text{Br}_x)_3$  with tunable bandgap and controlled morphology. The mixed-cation lead mixed-halide perovskites were deposited by simultaneous vacuum deposition of the precursors FAI, CsI,  $\text{PbI}_2$  and  $\text{PbBr}_2$ . In order to calibrate the deposition rate of each material, the specific tooling factors were determined by individually subliming them and comparing the thickness displayed from the quartz crystal microbalance (QCM) with the one measured with a mechanical profilometer. Unlike MAI, which exhibits non-standard sublimation properties, the FAI adhesion is rather independent on the chemical composition of the surface, and hence the FAI deposition rate can be monitored with a dedicated QCM placed nearby the corresponding thermal source. We prepared four perovskite compositions with increasing  $\text{Br}/\text{I}^-$  and  $\text{FA}^+/\text{Cs}^+$  ratios, with the aim to increase the bandgap while ensuring phase stability. After several variations, we found the following procedure to lead to the best performing perovskite compositions. The FAI and  $\text{PbI}_2$  deposition rates were kept constant at 0.8 Å/s and 1 Å/s, respectively. The  $\text{PbBr}_2$  deposition rate was varied from 0.07 to 0.22 Å/s, while the CsI rate was increased from 0.25 to 0.45 Å/s, to prevent halide segregation in the bromide-rich formulations.



*The PerTPV project has received funding from the European Union's Horizon 2020 research and innovation programme under grant agreement No 763977.*

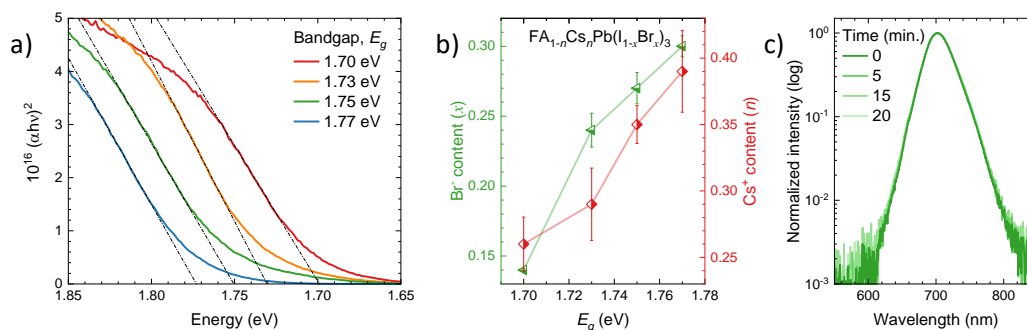


**Figure 1.1a.** (a) Tauc plot and estimated bandgap energies ( $E_g$ ) for a series of  $\text{FA}_{1-n}\text{Cs}_n\text{Pb}(\text{I}_{1-x}\text{Br}_x)_3$  perovskite films obtained with increasing the  $\text{PbBr}_2$  deposition rate. (b) Bulk bromide (left, green) and caesium (right, red) content in the perovskite films estimated by energy dispersive X-ray spectroscopy (EDS). (c) Normalized photoluminescence (PL) spectra of a representative sample (1.75 eV bandgap) recorded over time under continuous illumination. The excitation source is a 515 nm laser with an irradiance of approximately  $300 \text{ mW/cm}^2$ .

With increasing  $\text{PbBr}_2$  content (deposition rate), we observed the expected blue-shift of the absorption cutoff, indicating that indeed bromide is incorporated into the perovskite structure. The corresponding Tauc plots (Figure 1.1a) allow to estimate the bandgap energy of the four perovskite compositions, with  $E_g$  increasing steadily from 1.70 eV to 1.77 eV. The bulk  $\text{Cs}^+$  ( $n$ ) and  $\text{Br}^-$  ( $x$ ) concentrations in the different  $\text{FA}_{1-n}\text{Cs}_n\text{Pb}(\text{I}_{1-x}\text{Br}_x)_3$  samples were estimated by energy dispersive X-ray spectroscopy (EDS). As shown in Figure 1.1b, bromide and caesium contents were found to be in the  $0.14 \leq x \leq 0.30$  and  $0.26 \leq n \leq 0.39$  ranges, respectively. The  $\text{Cs}^+$  concentration was adjusted in order to stabilize the perovskite formulations against halide segregation, in particular when the bromide content is increased to obtain the wider-bandgap materials. In Figure 1.1c, the PL spectra of a perovskite film with  $E_g = 1.75 \text{ eV}$  is reported. Spectra were collected over time under continuous wave laser illumination (515 nm), at an irradiance of approximately  $300 \text{ mW/cm}^2$ , corresponding to a 5 – 6 sun equivalent intensity. Even with these harsh conditions, we did not observe any low energy PL components which would indicate halide segregation into iodide-rich regions. The perovskite films were further analysed by X-ray diffraction (XRD, Figure 1.2). The XRD data can be fitted considering a single distorted perovskite phase in combination with a marginal contribution from  $\text{PbI}_2$ , which is mostly visible by its main peak around  $2\theta = 12.8^\circ$ . All samples show a clear preferential orientation along the b-axis (perpendicular to the substrate), as evidenced by the two main reflections at  $2\theta = 14.2^\circ$  and  $2\theta = 28.7^\circ$ , which are ascribed to the (020) and (040) planes. The unit cell volumes derived from the whole-pattern Le Bail fits indicate a shrinkage of the unit cell from  $831.5 \text{ \AA}^3$  to  $821 \text{ \AA}^3$  as more iodide anions are replaced by bromide anions which have a smaller ionic radius. We also studied the morphology of the  $\text{FA}_{1-n}\text{Cs}_n\text{Pb}(\text{I}_{1-x}\text{Br}_x)_3$  thin films by SEM top view images (Figure 1.2). All films exhibit a similar surface morphology, composed of small grains (typical size in the 50-100 nm range) arranged in a compact and homogeneous manner. Such small grains are a common feature of vacuum deposited perovskite films.



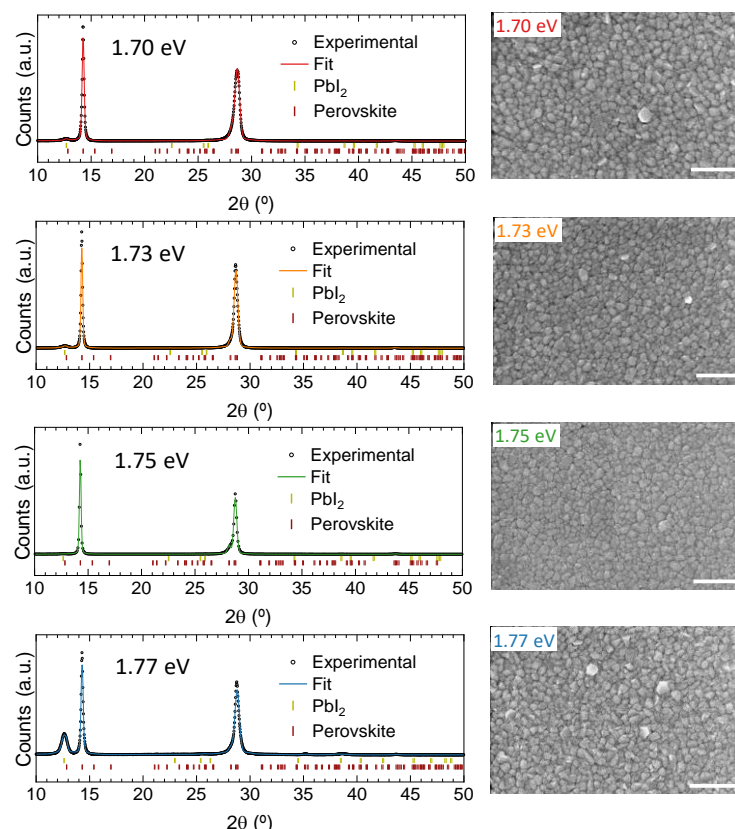


Figure 1.2. On the left, Whole-pattern Le Bail fit (coloured lines) of XRD patterns (open black circles). Vertical markers correspond to calculated Bragg's reflections for a distorted perovskite phase (dark red) and  $\text{PbI}_2$  (yellow). For each  $\text{FA}_{1-n}\text{Cs}_n\text{Pb}(\text{I}_{1-x}\text{Br}_x)_3$  sample, the corresponding surface morphology, as observed by SEM, is presented on the right, scale bar corresponds to 500 nm.

## 1.2 Vapour deposited low band gap Pb:Sn perovskite absorbers (UEG)

To-date, the only published routes for growing Pb:Sn perovskite films involve solution processing. However, vapour deposition may have many advantages, especially for multi-junction solar cells. The sublimation approach towards low bandgap perovskites carried out by UVEG is described here.

Two different processes were employed, co-sublimation and sequential sublimation, to prepare the Sn-Pb low bandgap perovskites. In the first all components were sublimed simultaneously whereas in the latter, first only the Sn and Pb salts were deposited by sublimation to later convert this in a wet process.

### Sn-Pb perovskite via co-sublimation:

To prevent oxidation of  $\text{Sn}^{2+}$  to  $\text{Sn}^{4+}$  all reports in the literature use the additive  $\text{SnF}_2$  in the preparation procedure, even its role is not completely understood. Hence, as a starting point we decided to also implement this in the co-sublimation route. For practical reasons, no more than 4 compounds can be co-evaporated at once (it is difficult to control the rates of the individual compounds with more materials subliming at the same time). Hence, with  $\text{SnF}_2$  three sources are left that can form the perovskite and if both Sn and Pb needs to be present that takes two more sources. We choose to focus on pure iodine perovskites thus we employed  $\text{SnI}_2$  and  $\text{PbI}_2$  as the starting compounds both supplied by TCI as highly pure materials. This leaves one source for the necessary A cation in the  $\text{ABX}_3$  perovskite structure. ( $\text{B} = \text{Sn-Pb}$ ,  $\text{X}=\text{I}$ ). Here we choose FA, as this was reported to be the most stable Sn-Pb perovskite.



The PerTPV project has received funding from the European Union's Horizon 2020 research and innovation programme under grant agreement No 763977.

However, due to the irreproducible performance of the solar cells with the  $\text{FASnPbI}_3$  perovskites with 10 % of  $\text{SnF}_2$ , alternative compositions were evaluated. The reason for the irreproducible results was not completely clear, however, the instability of the sublimation of FAI was one complicating factor in the thin film preparation, the unknown influence of the  $\text{SnF}_2$  was another.

Due to these disappointing results, different Sn-Pb composition were attempted, now without  $\text{SnF}_2$ . We chose a mixture of MA and Cs, as both MAI and CsI can be sublimed in a very reproducible way. This four component film is possible to prepare by simultaneously sublimation only if the  $\text{SnF}_2$  is left out. Like before, different crucible temperatures were set to determine off line which perovskite composition was obtained. By tuning the temperatures, we were able to go from an initial composition of  $\text{SnPbMACs}$  with a SnPb to MACs ratio of 1.2:1, to 2:1 and 2.3:1. The absorption spectra and XRD patterns of these compositions are shown in Figure 1.3.

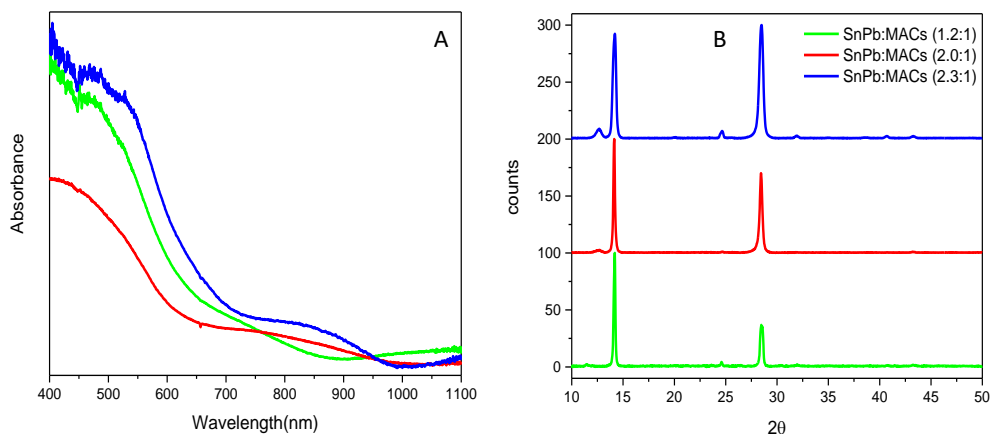


Figure 1.3. A: Absorption spectra and B XRD patterns of  $\text{MACsSnPbI}_3$  perovskites with different ratios between SnPb and MaCs.

Once established that the best crystallinity and best absorption was obtained for the films with a slight excess of SnPb compared to the A cations, different thicknesses of these films were prepared which were evaluated on the morphological and crystallinity. The XRD and SEM results are shown in Figure 1.4.

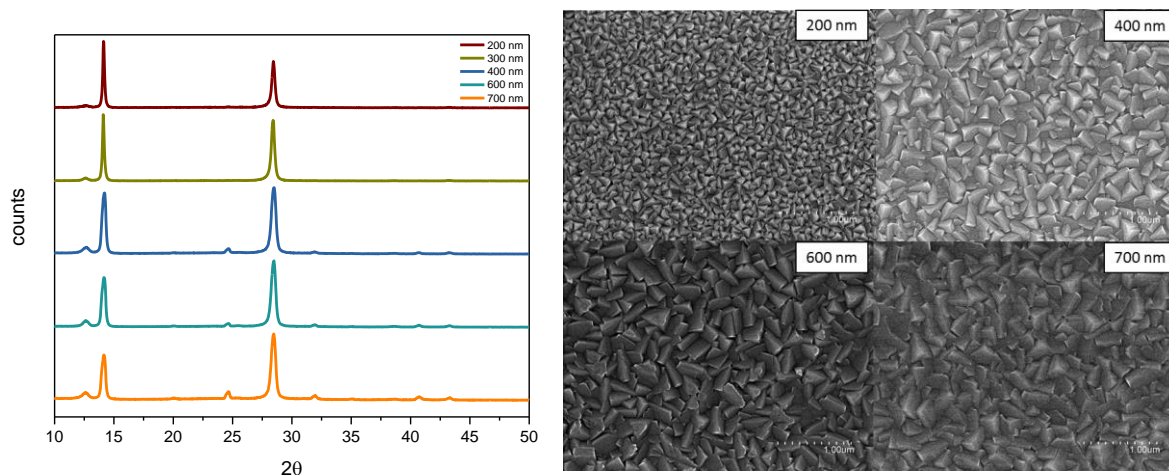


Figure 1.4 Left: XRD patterns of  $\text{MACsSnPbI}_3$  perovskites films with different thicknesses and Right: SEM top view images of the same films.





From these results it is clear that these films can be prepared in good reproducibility and that the grain size increases with increasing thickness. We are not sure why the latter is the case, obviously it takes longer to grow thicker films than thinner films and during sublimation the substrates may heat up slightly. Heating is the most logical cause for an increase in grain size, but as mentioned we are not sure. In our current setup we are unable to change the substrate temperature and we will try to change that in the near future by implementing new hardware.

The absorption of light increases with increasing thickness, yet the bandgap does not change notably as can be seen from Figure 1.5 The bandgap estimated from the Tauc plot is approximately 1.3 eV.

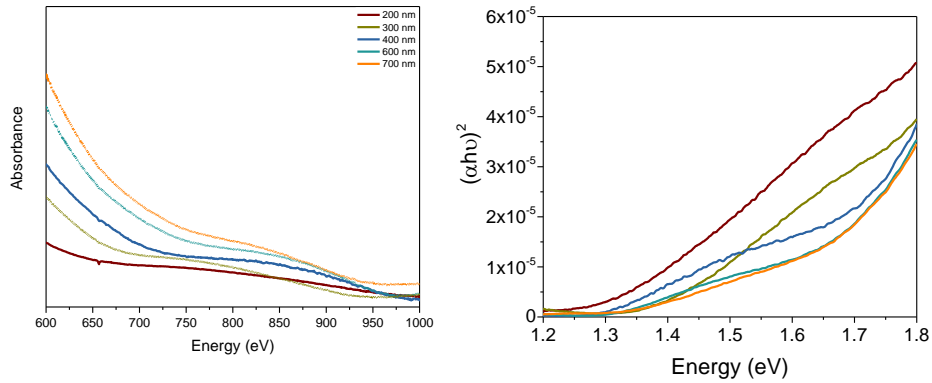


Figure 1.5. Left: Absorption spectra of MACsSnPbI<sub>3</sub> perovskites films with different thicknesses and Right: Tauc plots for the same films.

To verify the reproducibility of these films the variation in the bandgap as determined from Tauc plots and the composition determined by SEM-EDX were measured as a function of film thickness. The results are shown in Figure 1.6 and demonstrate a rather good control over the bandgap and composition significantly improved compared to the FA based SnPb perovskites.

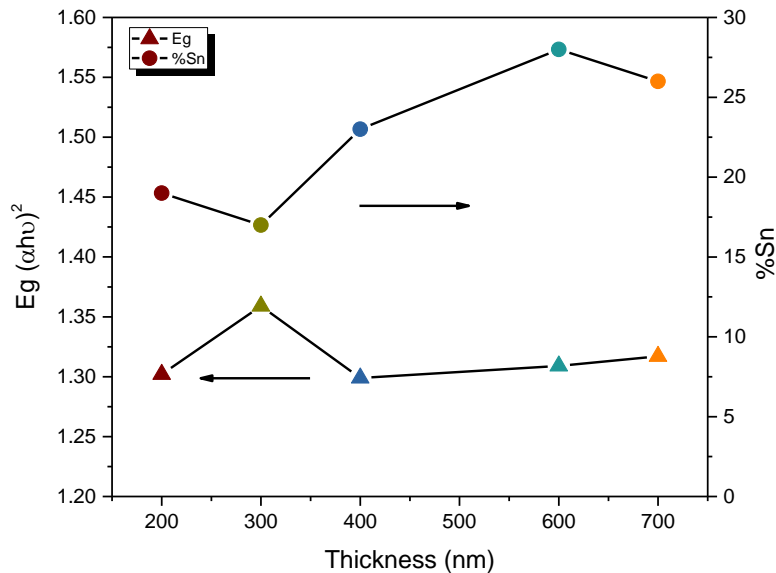


Figure 1.6. Bandgap and composition variation as a function of MACsSnPbI<sub>3</sub> film thickness.



### Sn-Pb perovskite via sequential-sublimation:

To maximize the possibilities for Sn-Pb perovskite preparation parallel to the co-sublimation route, we also investigated the sequential deposition route, in which first the two B metal salts were co-sublimed to form a (Sn-Pb)I<sub>2</sub> film which than is post converted using a solvent based step where the A cation is added. This reduces the complexity in the sublimation route as both SnI<sub>2</sub> and PbI<sub>2</sub> sublime in a controlled manner with a nice cone preventing cross-talk between the sensors. Additionally, the A cations can more easily be varied as they are dissolved in isopropanol. The difficulty, with this method is how to ensure full conversion of the (Sn-Pb)I<sub>2</sub> film by depositing the A cation solution. Also, here the use of SnF<sub>2</sub> and its role is not clear. In Figure 1.7 SEM images of the (Sn-Pb)I<sub>2</sub> film and the FaSnPbI<sub>3</sub> films are shown.

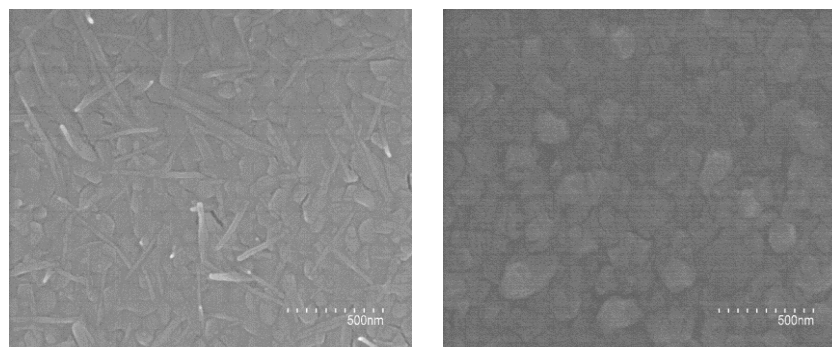


Figure 1.7. SEM top images of: Left before conversion (PbI<sub>2</sub> + SnI<sub>2</sub>), middle: after conversion (FAPbSnI<sub>3</sub>).

From the SEM images a clear change is observed indicating the formation of the low bandgap perovskite. The degree of conversion cannot be assessed from this data and therefore, absorption spectra and X-ray diffraction patterns were taken for different conditions (amount of FAI isopropanol solution). In Figure 1.8 the different stages can be clearly observed in both absorption spectra and XRD patterns. Most importantly it is possible to obtain complete conversion, at least to the limit of the detection of XRD as for green diffractogram shows no signs of (Sn-Pb)I<sub>2</sub> remains.

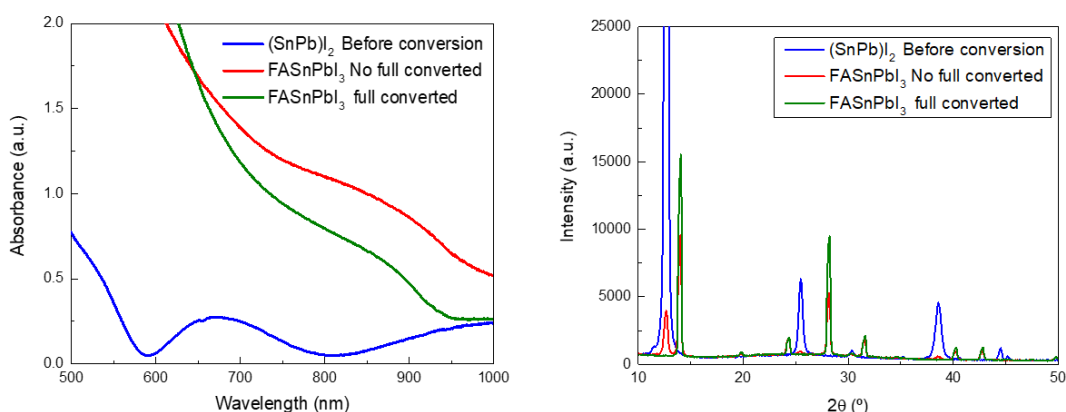


Figure 1.8. Following conversion of (Sn-Pb)I<sub>2</sub> films. Left: absorption spectra and Right: XRD patterns.

Similar to what we did for the co-deposited FASnPbI<sub>3</sub> perovskites, also for the sequentially deposited version we determined the conductivity by depositing them on top interdigitated electrodes. As can be seen in Figure 1.9, the conductivity is much higher than for the co-deposited samples. This we attribute to a significant amount of Sn<sup>4+</sup>, which is most likely originating from small amount of water/oxygen molecules in the glovebox where the conversion is carried out. We did continue with the preparation of





solar cells as described in WP2, yet the results were disappointing with efficiencies below 5%.

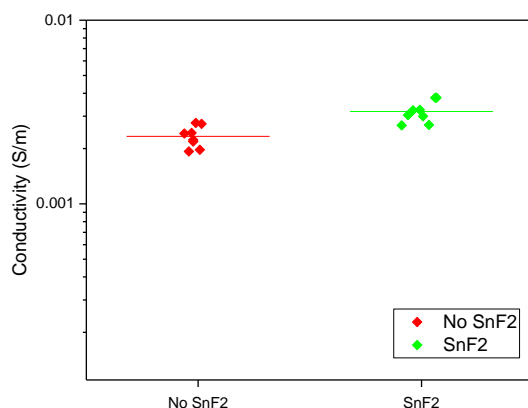


Figure 1.9. Conductivity of  $\text{FASnPbI}_3$  perovskites prepared by sequential deposition with and without  $\text{SnF}_2$  co-sublimed with the Sn and Pb salts.

We then spend extra efforts to exclude moisture during the process, by maintaining a more rigorous purging regime in the glovebox, replacement of the drying materials in the column. Also, we adopted a different method to convert the  $(\text{Sn-Pb})\text{I}_2$  films by not only adding the iodide salt of FA, but also small amounts of its Cl and Br salts. From a comparison study using  $\text{PbI}_2$ , we learned that the addition of these other halide salts increased the conversion to perovskite and allowed for the use of thicker seed layers.

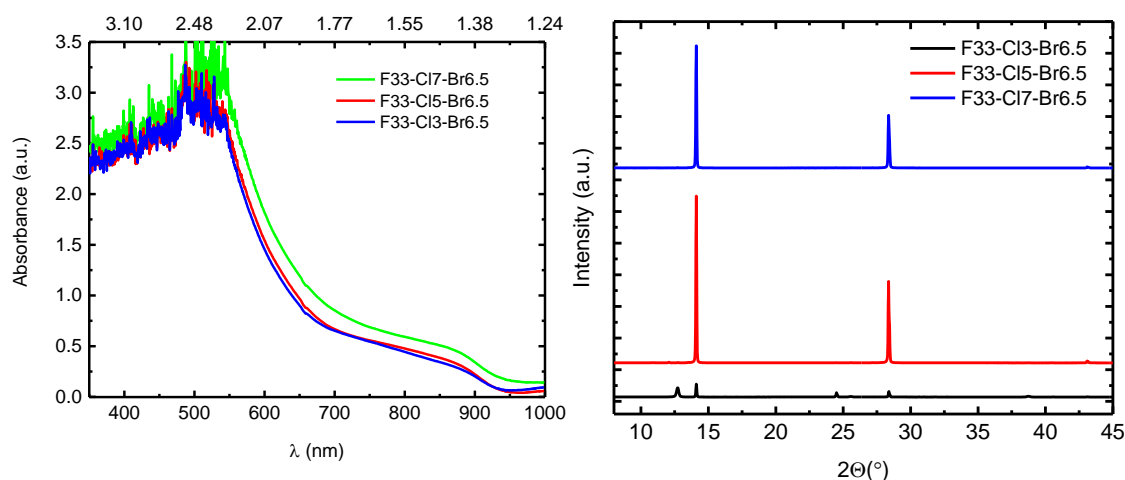


Figure 1.10. Following conversion of  $(\text{Sn-Pb})\text{I}_2$  films. Left: absorption spectra and Right: XRD patterns.

From the results in Figure 1.10, indeed it can be observed that these sequentially prepared  $\text{FASnPbI}_3$  perovskites, have an increased absorption spectrum and a much more defined XRD pattern, both indicating complete conversion up to thicknesses of 450 nm.

### 1.3 Solution processed narrow band gap absorber (UOXF)

We have investigated a range of compositions for the Pb:Sn perovskite and have found that good quality material can be obtained with Pb:Sn ratio's varying between 70:30 to



The PerTPV project has received funding from the European Union's Horizon 2020 research and innovation programme under grant agreement No 763977.

40:60. In Figure 1.12 we show how the band gap of the Pb:Sn perovskite varies with the percentage of Sn added.

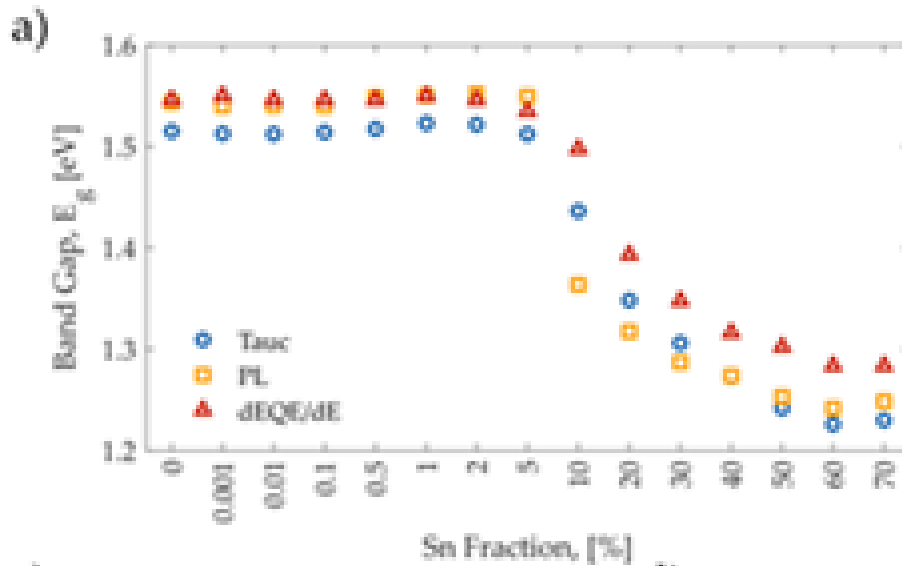


Figure 1.11. Band gap versus Sn composition for the  $FA_{0.83}Cs_{0.17}Pb_ySn_{1-y}I_3$

We have fixed the composition at 50:50 Pb:Sn, which delivers close to the lowest band gap possible, while also retaining good stability. We have managed to achieve a Tauc band gap of 1.24 eV and a d(EQE)/dE (or so called PV-band gap) of 1.3 eV (Figure 1.11) by spin-coating  $FA_{0.83}Cs_{0.17}Pb_{0.5}Sn_{0.5}I_3$  Perovskite from a 4:1 DMF:DMSO solution.  $SnF_2$  is added to suppress the deleterious oxidation of  $Sn^{2+}$  to  $Sn^{4+}$ . In Figure 1.12 we show the optical properties of this material.

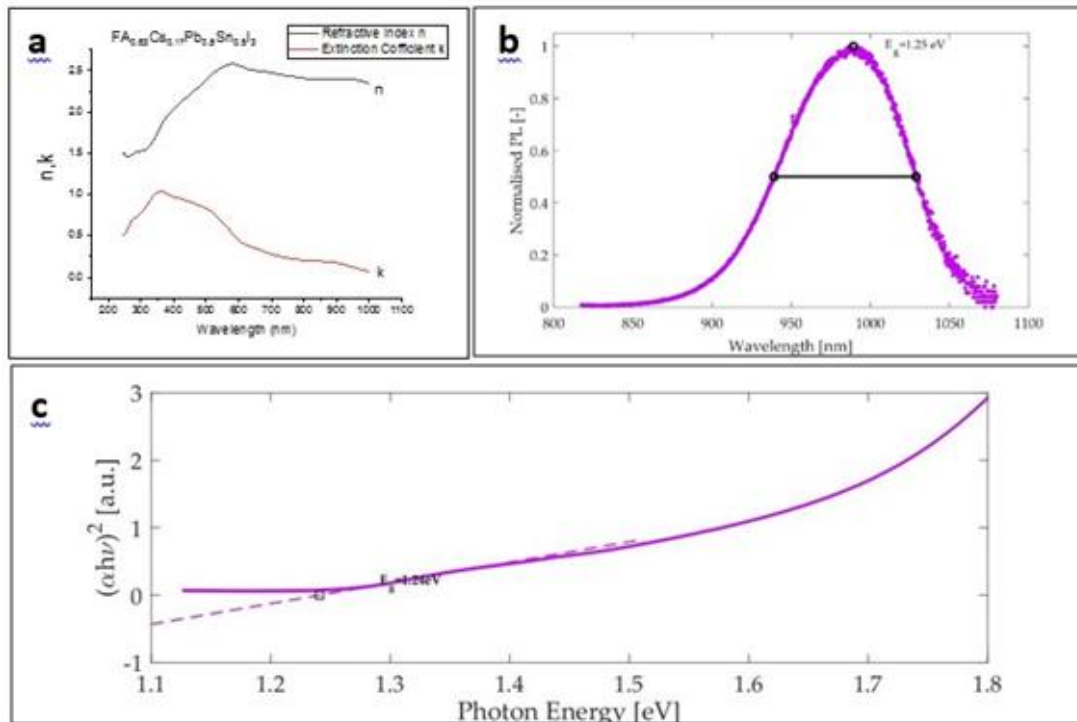


Figure 1.12  $FA_{0.83}Cs_{0.17}Pb_{0.5}Sn_{0.5}I_3$  perovskite material properties; (a) optical constants, (b) photoluminescence spectra and (c) Tauc plot from the UV-Vis absorption spectra.



## 1.4. Solution processed wide band gap absorber (UOXF)

It is well known that the bandgap of lead perovskites can be tuned between 1.6-2.3 eV by changing the iodide/bromide ratio. To achieve a perovskite material having a bandgap of 1.8 eV, we tune the stoichiometry of the perovskite precursor solution to be  $\text{FA}_{0.83}\text{Cs}_{0.17}\text{Pb}(\text{I}_{0.8}\text{Br}_{0.4})_3$ . To obtain the film, we adopted the 'solvent-quenching' approach which involves dripping an anti-solvent (Anisole in this case) upon the film while the film is spinning. After the spin, the film was immediately transferred to a hotplate preheated to 100 °C for 1 hour. To examine if we get the right bandgap, we measure the absorption spectrum of the well-crystallised  $\text{FA}_{0.83}\text{Cs}_{0.17}\text{Pb}(\text{I}_{0.8}\text{Br}_{0.4})_3$  film and performed Tauc plot analysis to extract the bandgap (Figure 1.13(a) and (b)). We obtained the right bandgap of 1.8 eV. This is also in agreement with the optical constants measured using ellipsometry (Figure 1.14). We further examine the optoelectronic properties of this perovskite material by measuring the photoluminescence spectrum (Figure 1.13(c) and (d)). The photoluminescence spectrum shows a peak centred at 690 nm, which agrees with the bandgap obtained from the absorption measurement.

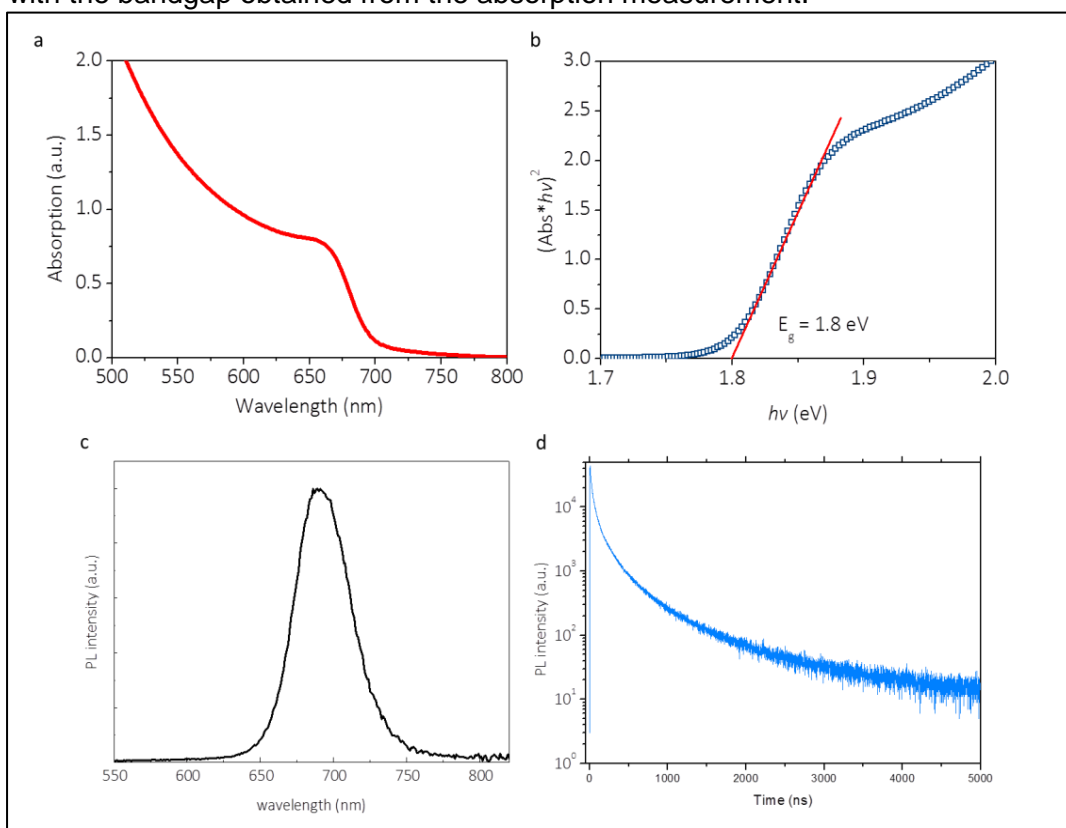


Figure 1.13 (a) Absorption spectrum of the  $\text{FA}_{0.83}\text{Cs}_{0.17}\text{Pb}(\text{I}_{0.8}\text{Br}_{0.4})_3$  perovskite film. (b) Corresponding Tauc plot determining the bandgap of the perovskite film. (c) Photoluminescence (PL) spectrum. (d) Time-resolved photoluminescence.



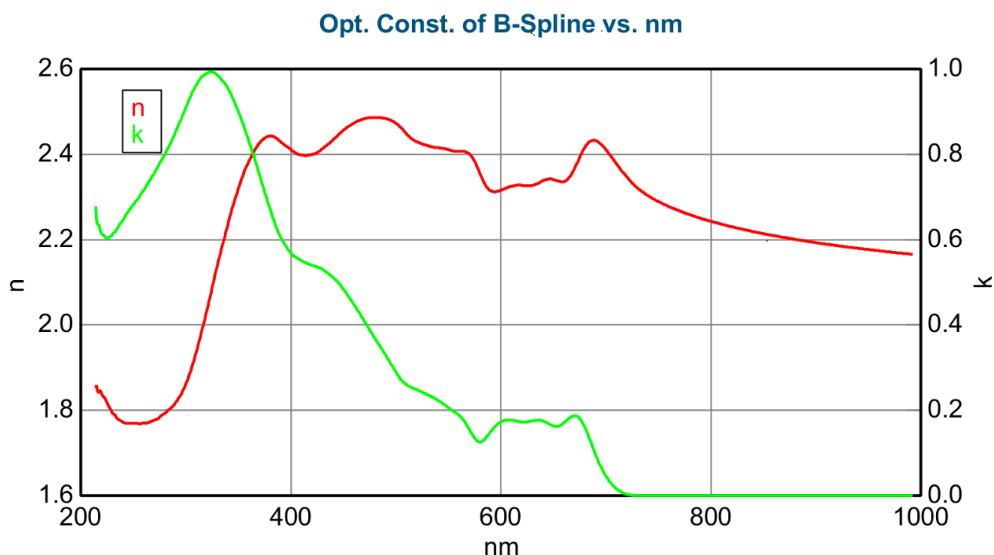


Figure 1.14. Optical constants of a spin-coated high bandgap  $FA_{0.83}Cs_{0.17}Pb(I_{0.4}Br_{0.6})_3$  perovskite obtained using spectroscopic ellipsometry.

To enhance the properties of the wide band gap absorber, we found that “doping” the material with piperidinium salts, has resulted in dramatic improvements. In Figure 1.15 we show the additive and the device stack.

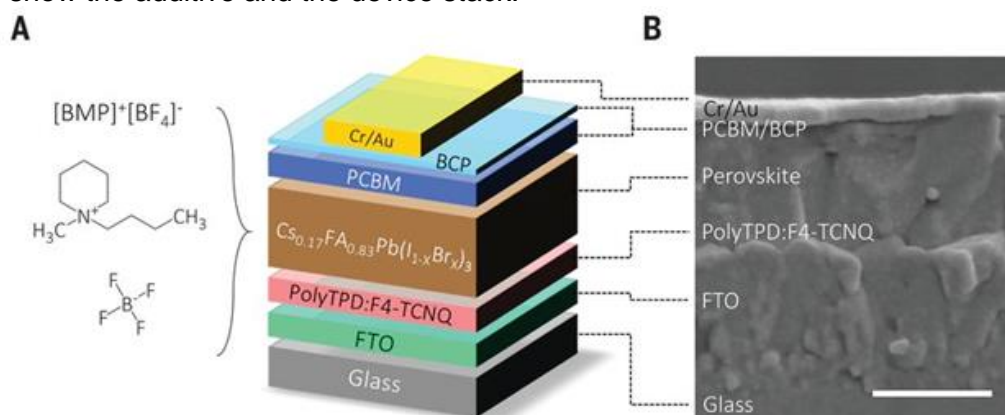


Figure 1.15. (a) Device structure and piperidinium salt additive added to the perovskite films. (b) Scanning electron microscopy cross sectional image of such a device.

In Figure 1.16, we show the determined quasi-fermi level splitting (QFLS), which is analogous to the open-circuit voltage, of the 1.8 eV perovskite absorber layer on different substrates. What is very interesting here, is that the piperidinium salt does improve the QFLS of the isolated perovskite film coated on glass, but it has an even stronger more positive effect when the perovskite films are in contact with either the hole-transport materials (PTAA and polyTPD) or the electron transport material ( $C_{60}$ ). This indicates that this additive greatly suppresses non-radiative recombination at the heterojunctions, and hence holds the potential to deliver greatly enhanced open-circuit voltages in the solar cells.



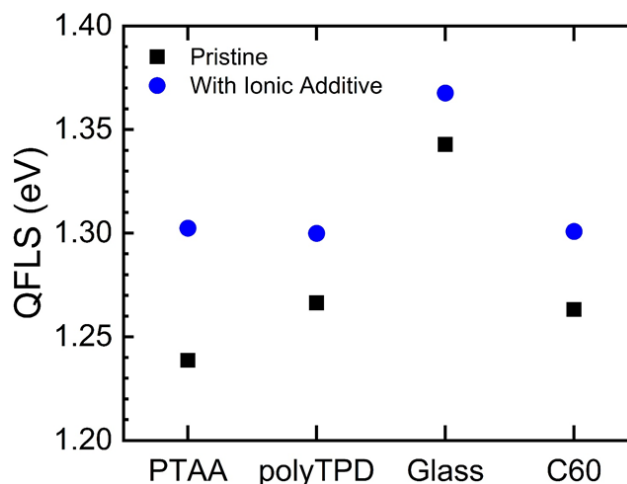


Figure 1.16: Quasi-Fermi Level Splitting (QFLS), determined from PLQE measurements, of 1.8 eV perovskite films with (blue circles) and without (black squares) piperidinium ionic additive, coated upon poly(triarylamine) (PTAA), poly(triphenyldiamine) (polyTPD), glass, and C<sub>60</sub>.

## 2. Development of n-type materials

### 2.1. Alternative non-fullerene ETMs for vacuum deposited devices (UEG)

Fullerene derivatives are exceptional ETMs and electron acceptors for narrow bandgap solar cells. However, when the perovskite bandgap is increased as needed for front sub-cells in tandem devices, fullerenes might become a recombination centers due to the comparable optical bandgaps of the fullerene and the perovskite. For example, looking at the EQE response in the bandgap region of a p-i-n cell based on the wide bandgap perovskite CsPbI<sub>2</sub>Br ( $E_g = 1.9$  eV, Figure 2.1a), one can observe an additional component at low energies (at 1.7 eV), which corresponds to carrier photo-generation by the C<sub>60</sub> itself.

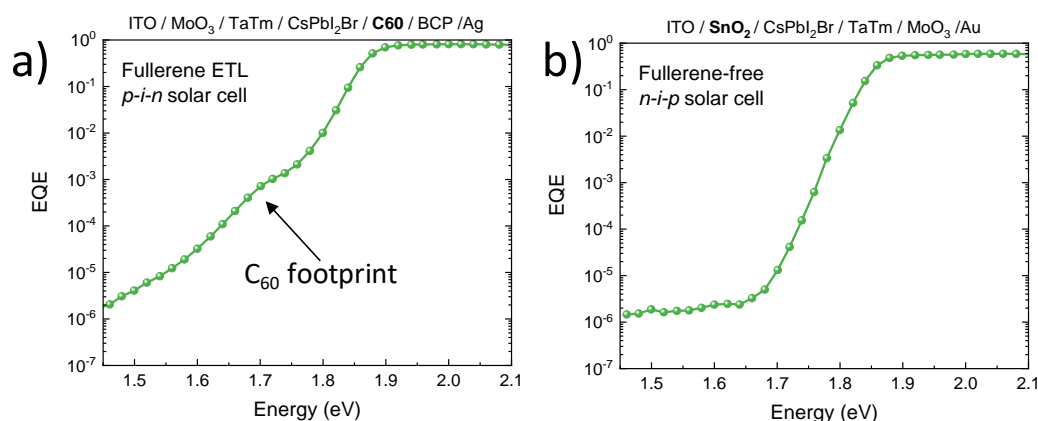


Figure 2.1. EQE response in the bandgap region for wide bandgap (1.9 eV) perovskite solar cells in the p-i-n and n-i-p configurations, using C<sub>60</sub> or SnO<sub>2</sub> as the ETMs, respectively.

This is also confirmed by the spectral response of inverted n-i-p cells with the same perovskite but using only SnO<sub>2</sub> as the ETMs (Figure 2.1b). Being a wide bandgap semiconductor ( $E_g \approx 3$  eV), SnO<sub>2</sub> allows to extract electrons without interfering with carrier generation. As unavoidable in any semiconductor, if carrier generation occurs



there will be also carrier recombination, and hence  $C_{60}$  might account for a voltage loss in perovskites with  $E_g > 1.7$  eV.

Hence, wide bandgap perovskite requires ETMs with bandgaps  $> 2$  eV and favorable band alignment, i.e. the ETLs LUMO should be aligned with or only slightly below the perovskite conduction band. Unfortunately, organic ETMs with high electron affinity and wide bandgap are not common. We have searched the scientific literature and identified few commercial candidates which fulfil the above-mentioned requirements. Specifically, only small molecular weight materials were scrutinized, as they can be sublimed and readily implemented in tandem devices.

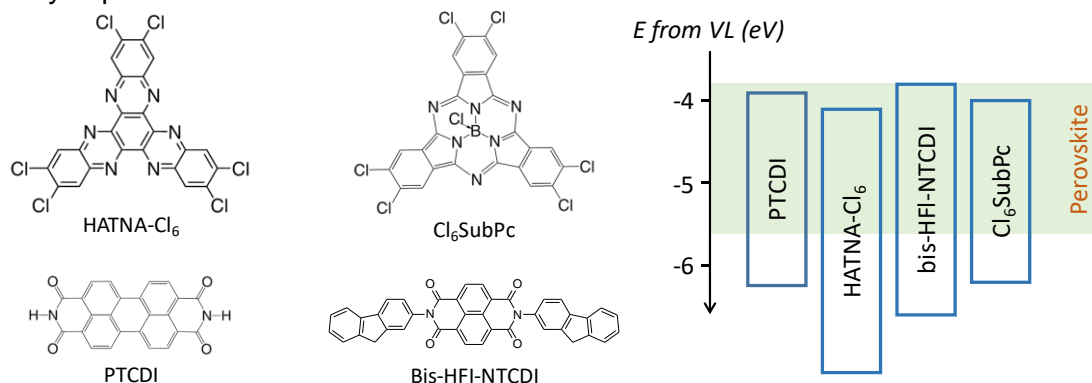


**Figure 2.2.** Chemical structure and schematic flat band energy diagram for a series of wide bandgap ETMs with high electron affinity. The green area approximates the positions of the valence and conduction bands for a wide bandgap ( $> 1.7$  eV) perovskite. All data are taken from literature.

The selected ETMs are 2,3,8,9,14,15-Hexachlorodiquinoxalino[2,3-a:2',3'-c]phenazine (HATNA- $Cl_6$ ), 2,3,9,10,16,17-Hexachlorinated boron subphthalocyanine chloride ( $Cl_6$ SubPC), 3,4,9,10-Perylenetetracarboxylic diimide (PTCDI) and *N,N*-bis(fluorene-2-yl)-naphthalenetetracarboxylic diimide (Bis-HFI-NTCDI). Their chemical structure and the absolute values of the frontier orbitals are reported in Figure 2.2.

The ETMs were tested in p-i-n perovskite solar cells with the structure ITO/MoO<sub>3</sub> (5 nm)/TaTm (10 nm)/perovskite (500 nm)/ETM/BCP (8 nm)/Ag, where TaTm is the hole transport material (HTM) *N,N,N',N'*-Tetra([1,1'-biphenyl]-4-yl)[1,1':4',1''-terphenyl]-4,4''-diamine, BCP is the electrode interlayer bathocuproine, and the perovskite is a vacuum processed film of composition  $FA_{0.65}Cs_{0.35}Pb(I_{0.73}Br_{0.27})_3$  with a bandgap  $E_g = 1.75$  eV. The reference samples use  $C_{60}$  (25 nm) as the ETM. We initially tested HATNA- $Cl_6$  as the ETM, using very thin films (either 5 or 10 nm) in view of the low reported charge mobility for this specific compound. The current-density vs. voltage (J-V) curves under illumination (Figure 2.3a) for the solar cells employing HATNA- $Cl_6$  as the ETM show strongly hindered charge extraction, with low FF and  $J_{sc}$  as compared to the reference with  $C_{60}$ . Hysteresis in the J-V curve when scanning in forward (from short- to open-circuit) and reverse (from open- to short-circuit) bias is also present, which is most likely indicative of a mismatch in the electronic energy levels between the perovskite and HATNA- $Cl_6$ , resulting in charge accumulation in one of the two scan direction. Hindered charge injection can be observed for the dark J-V curves (Figure 2.3b), where the built-in potential and maximum current densities are lower compared to the reference solar cells.





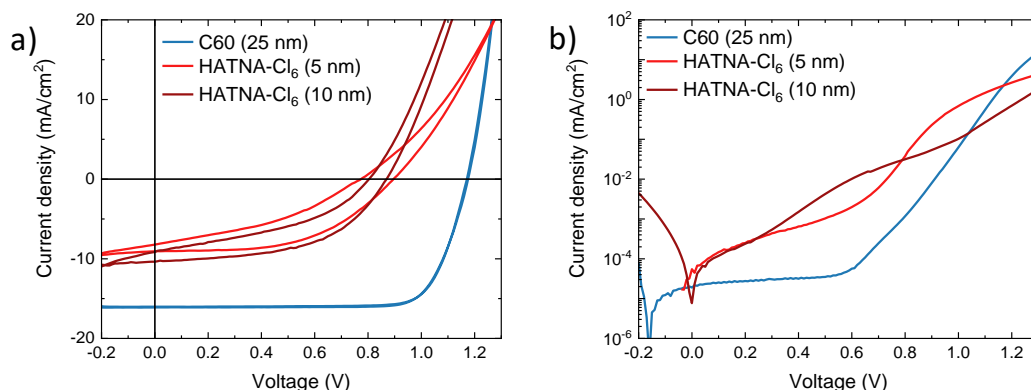


Figure 2.3. J-V curves measured under illumination (a) and in the dark (b) for solar cells employing the reference C<sub>60</sub> and HATNA-Cl<sub>6</sub> as the ETMs.

The hindered charge injection/extraction also led to severe non-radiative charge recombination (most likely at the very same ETM/perovskite interface), which lower the open circuit voltage ( $V_{oc}$ ) as compared to the reference (890 mV vs. 1175 mV for HATNA-Cl<sub>6</sub> and C<sub>60</sub>, respectively). We then studied the potential of Bis-HFI-NTCDI as ETM in wide bandgap solar cells, again using thin layers of this compound in between the perovskite and BCP. Also with this ETM, we observed a lower FF as compared to the reference, although the  $J_{sc}$  was recovered if using a 5 nm thick Bis-HFI-NTCDI film (Figure 2.4). We also observed lower hysteresis at open-circuit as compared to cells with HATNA-Cl<sub>6</sub>, as well as similar  $V_{oc}$  among Bis-HFI-NTCDI and C<sub>60</sub>, which might indicate that there is less electronic mismatch between the perovskite and the ETMs.

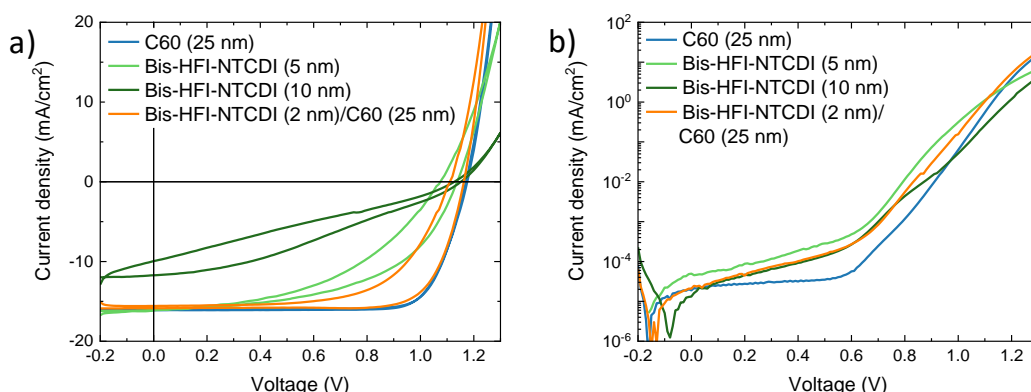


Figure 2.4. J-V curves measured under illumination (a) and in the dark (b) for solar cells employing the reference C<sub>60</sub> and Bis-HFI-NTCDI as the ETMs.

We further tested the potential of Bis-HFI-NTCDI in vacuum-deposited perovskite solar cells by employing an even thinner layer (2 nm) in combination with C<sub>60</sub>. We found that the J-V curve for this ETM combination closely resembled the one of reference solar cells with only C<sub>60</sub>. J-V hysteresis was still present, which again points at a mismatch in the energy level alignment between the wide bandgap perovskite and Bis-HFI-NTCDI. We used the same configuration, i.e. ETM (2 nm)/C<sub>60</sub> (25 nm), to test the last two ETMs selected in these series, Cl<sub>6</sub>SubPC and PTCDI. The corresponding J-V curves measured under illumination and in the dark are represented in Figure 2.5.



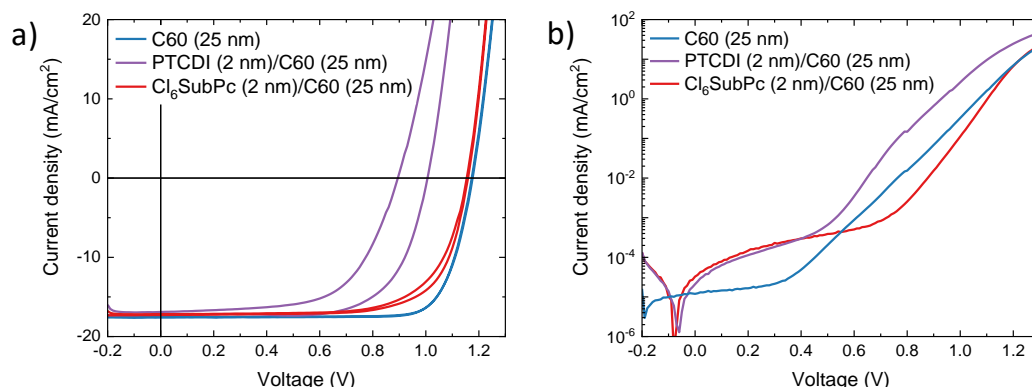


Figure 2.5. J-V curves measured under illumination (a) and in the dark (b) for solar cells employing the reference  $C_{60}$  and PTCDI or  $Cl_6SubPc$  as the ETMs.

In these cases, the maximum photocurrent measured for the device series was overall similar, implying that using only 2 nm thick ETMs allows for efficient charge carrier extraction at short circuit, as also observed with Bis-HFI-NTCDI. In the case of PTCDI, J-V hysteresis was rather severe, as well as non-radiative losses at open-circuit, causing a very low  $V_{oc}$  in the 0.8-1.0 V range depending on the scan direction. On the other hand, devices with  $Cl_6SubPc$  showed only negligible J-V hysteresis, and the device performance was mainly limited by a low FF with only minor voltage losses.

As a summary, thin Bis-HFI-NTCDI and  $Cl_6SubPc$  in combination with  $C_{60}$  underperformed as compared to  $C_{60}$  (PCE of 15.3, 13.9 and 16.5 % for devices with Bis-HFI-NTCDI,  $Cl_6SubPc$  and  $C_{60}$  accordingly). The photovoltage of the corresponding solar cells is rather similar (1.170 V and 1.168 V for Bis-HFI-NTCDI and  $Cl_6SubPc$  vs 1.171 V for  $C_{60}$ ), indicating that these materials do not bring additional non-radiative recombination channels. In general, the materials remain promising, and doping strategies could be used to compensate for the low FF observed.

## 2.2. Alternative naphthalenetetracarboxylic diimide ETMs (KTU)

As described in the previous chapter, it is important to search for more efficient electron transporting materials that ideally do not absorb light in the same spectral range as perovskite. For this task we have chosen to investigate naphthalenetetracarboxylic diimide (NDI) derivatives, which have shown their electron transporting capabilities in other optoelectronic applications. Investigation of these materials was conducted in two directions: NDIs capable of forming self-assembled monolayers and NDIs suitable for vacuum-deposition. In addition to low material consumption minimal parasitic absorption and relative ease of deposition, the SAM NDIs would also be less prone to solubility and crystallinity problems plaguing many electron transporting materials. Furthermore, NDIs are relatively straightforward to synthesize, which could not be said about many other ETMs.

Electron transporting materials capable of forming SAMs were obtained using a one-pot synthesis technique. Compounds were synthesized *via* successive reactions without isolation of intermediates. As an example, synthesis of a new semiconductor containing pyridine anchoring group and a protective pentafluorophenyl moiety at 2 and 7 positions of naphthalenetetracarboxydimide was obtained by condensing 1,4,5,8-naphthalenetetracarboxide anhydride with 2,3,4,5,6-pentafluoranyliline in DMF at 120 °C. The intermediate obtained during the synthesis was used in the next reaction step without isolation from the reaction mixture. The intermediate is condensed with 4-aminopyridine to form NDI derivative **V1242** (Figure 2.6).



The PerTPV project has received funding from the European Union's Horizon 2020 research and innovation programme under grant agreement No 763977.

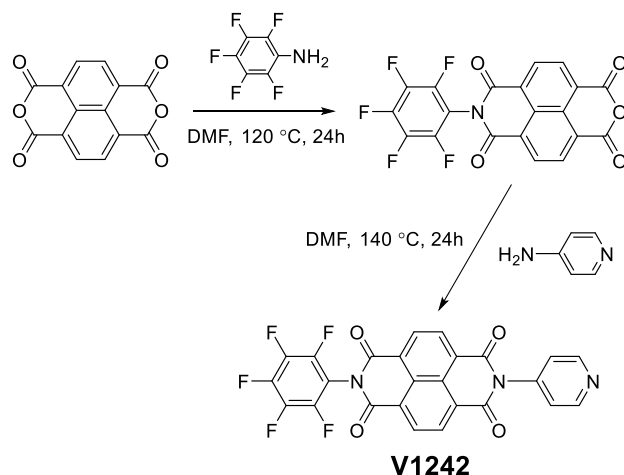


Figure 2.6. One-pot synthesis of NDI derivative **V1242** with pyridine anchoring group.

Derivatives **V1210**, **V1266** were obtained in the same manner, although compound **V1210** required an extra step to form the actual anchoring group (Figure 2.7).

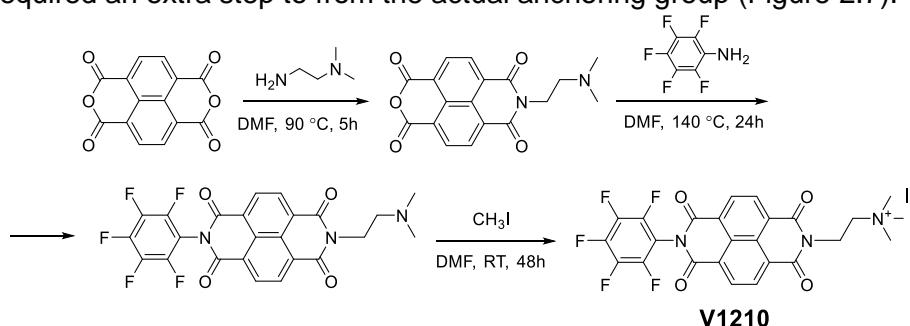


Figure 2.7. Synthesis of NDI derivatives with quaternary ammonium cation group.

Other group of the NDI materials was synthesized with the aim to utilise them in vacuum-deposited PSC devices. These molecules were obtained in a similar fashion as the ones discussed earlier, although the synthesis itself is simpler and faster as molecules are symmetrical and only one synthesis step is needed (Figure 2.8).

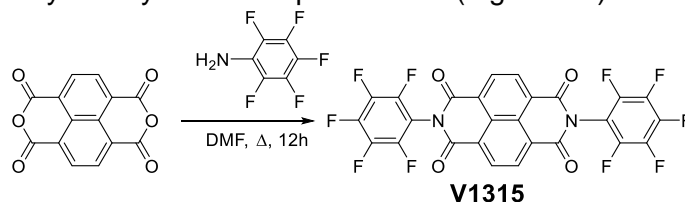


Figure 2.8. Synthesis of symmetric NDI derivative with pentafluorophenyl groups.

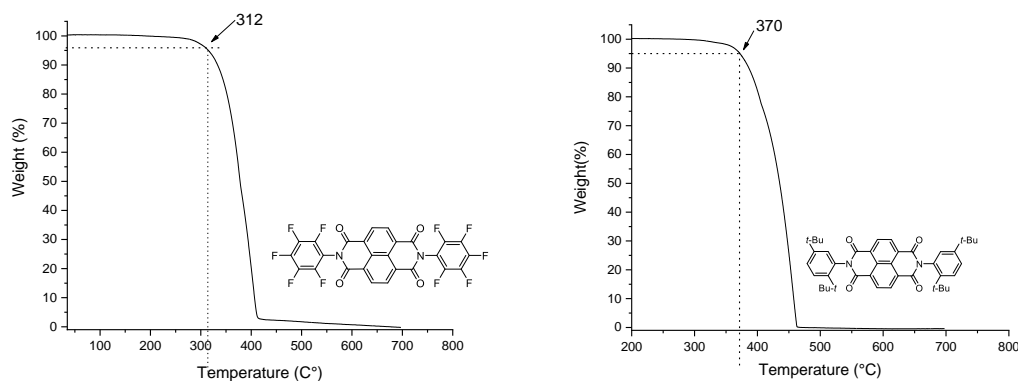
Structures of the investigated NDI derivatives are depicted in Table 2.1. Thermal gravimetry analysis of the compounds indicates that molecules with anchoring groups mostly tend to undergo thermal decomposition at lower temperatures than symmetric derivatives developed for vacuum-deposition (**V1314**, **V1315**, **V1316**). However, these temperatures are sufficient for practical application in perovskite solar cells.



Table 2.1. Thermal properties of naphthalenedetracarboxydimides

No.	Structure	$T_{\text{dec}}, ^\circ\text{C}$
<b>V1242</b>		315
<b>V1210</b>		241
<b>V1266</b>		198
<b>V1314</b>		411
<b>V1315</b>		312
<b>V1316</b>		370

Thermogravimetric analysis results of the two most promising symmetric NDI derivatives **V1315**, **V1316** are shown in Figure 2.9. The tested materials demonstrated 5% weight loss above 300 °C, proving that they are sufficiently thermally stable for application in PSCs. Furthermore, the rapid weight loss seen in Figure 2.9 suggests that the investigated materials can readily evaporate and demonstrate potential for vacuum deposition.

Figure 2.9. TGA heating curves of **V1315** and **V1316**.

To evaluate energy levels of the new compounds electron affinity was calculated using cyclic voltammetry CV measurements data (Table 2.2). NDI derivatives demonstrate  $E_{\text{LUMO}}$  in the interval of 3.8-4.3 eV, providing a relatively wide range of energy levels for optimization for various perovskite compositions. Interestingly, pentafluorophenyl and quaternary ammonium groups provide the biggest shifts in  $E_{\text{LUMO}}$ .



The PerTPV project has received funding from the European Union's Horizon 2020 research and innovation programme under grant agreement No 763977.

Table 2.2. Light absorption and electrochemical characteristics and of naphthalenedetracarboxydimides

No.	Structure	$\lambda$ , nm	$E_{\text{HOMO}}$ , eV	$E_{\text{LUMO}}^a$ , eV	$E_g^b$ , eV
<b>V1242</b>		387	-7.3	-4.10	3.2
<b>V1210</b>		387	-7.51	-4.31	3.2
<b>V1266</b>		390	-7.27	-4.09	3.18
<b>V1315</b>		386	-7.21	-4.0	3.21
<b>V1316</b>		391	-6.99	-3.82	3.17

<sup>a</sup> Electron affinity data obtained from CV measurements in solution; <sup>b</sup>  $E_g$  from absorbance spectra (in the solution). Results in the solid films might differ.

Preliminary testing has been conducted with both ETMs suitable for vacuum deposition and SAM ETMs. SAM ETMs have been tested in two different device architectures. NDI ETM **V1210** have been used in ITO/NiO<sub>x</sub>/MeO-PACz/Perovskite/V1210/BCP/Ag. Unfortunately, device performance was lagging significantly behind standard C<sub>60</sub>. PSC with **V1210** have demonstrated power conversion efficiency of just 2-4%, compared with PCE of 18 % recorded using C<sub>60</sub>. The other two SAM ETMs (**V1266**, **V1242**) have been investigated using PSC with architecture ITO/ MeO-2PACz/ Perovskite/ V1266 or V1242/ BCP/ Cu. These materials performed a little better (PCE = 10-12%), however, performance difference between new NDI SAMs and C<sub>60</sub> remains significant, PSC with C<sub>60</sub> has demonstrated PCE=20.2 %. Although, it has to be said that device constructed without ETM layer (ITO/ MeO-2PACz/ Perovskite/ BCP/ Cu) has registered PCE of 5.4 %. Therefore, we can conclude that investigated NDI SAM do function as electron transporting layers, however further structure and energy level optimization is necessary to improve overall device performance.

### 3. Development of p-type materials

The aim of this part of the work is development of new hole-transporting materials (HTMs) with energy levels designed to match the wide bandgap perovskite absorber materials from Task 1.1 that can be used in solution-based deposition and vacuum sublimation methods. Ionisation potential of the developed HTMs ideally should be in the range between 5.2 and 5.7 eV for wide bandgap absorbers, and 4.8 to 5.1 eV for narrow bandgap absorbers.

#### 3.1. Shallow HOMO hole transporting materials (KTU)

##### 3.1.1 Spirobifluorene and fluorene-based derivatives



The PerTPV project has received funding from the European Union's Horizon 2020 research and innovation programme under grant agreement No 763977.

We have investigated Spiro-OMeTAD analogues, with the methoxyphenyl and carbazole groups changed to the spirobifluorene core. In addition, materials with simpler “half” structures were investigated, where 9,9- positions of the fluorene moiety are occupied by different alkyl chains.

Synthesis of these hole transporting materials was conducted via Buchwald-Hartwig amination. Commercially available 2,2',7,7'-tetrabromo-9,9'-spirobifluorene and 2,7-dibromofluorene were used as precursors for the synthesis of spiro-based (Figure 3.1) “half” analogues (Figure 3.2) accordingly. These starting materials were coupled with 9-ethyl-*N*-(4-methoxyphenyl)-9*H*-carbazol-3-yl-amine, to give target compounds **V1222**, **V1226**, **V1238**, **V1240**, and bis(9-ethyl-9*H*-carbazol-3-yl)amine, to yield **V1257**, **V1258**, **V1267**, **V1269**.

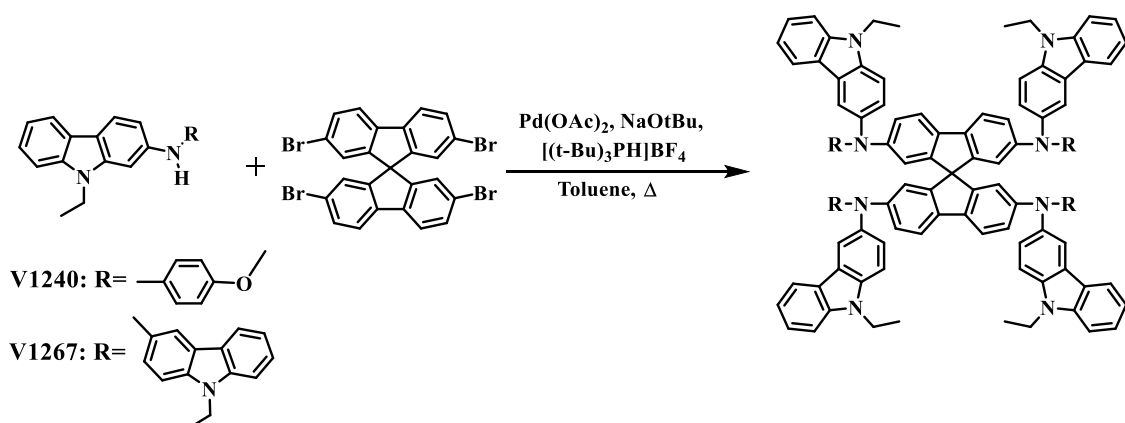


Figure 3.1. Synthesis of the spirobifluorene derivatives **V1240** and **V1267**.

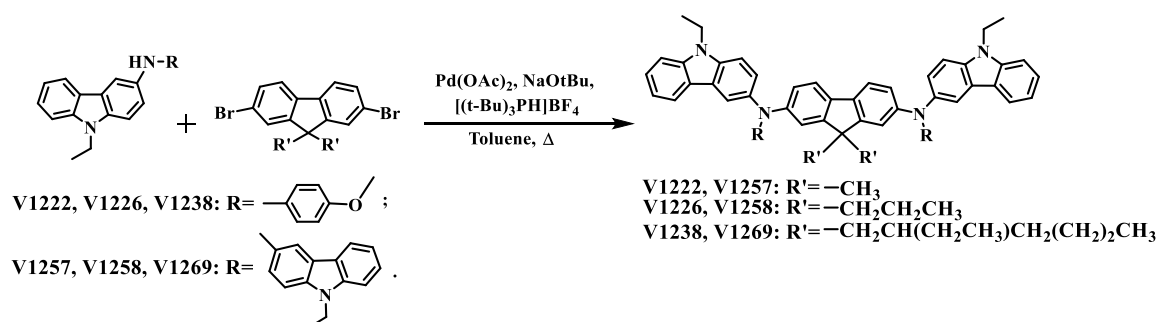
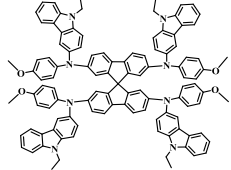
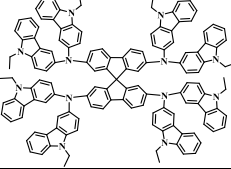
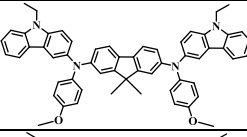
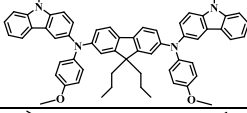
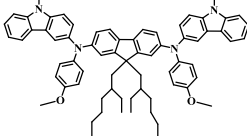
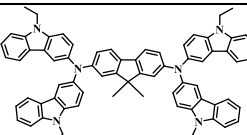
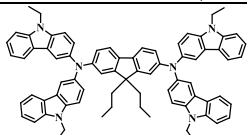
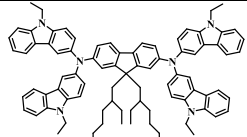


Figure 3.2. Synthesis of the fluorene compounds **V1222**, **V1226**, **V1238**, **V1257**, **V1258**, and **V1269**.





Table 3.1. Thermal and photophysical properties of the synthesized materials

	Compound	$T_g$ , <sup>a</sup> °C	$T_{dec}$ , <sup>b</sup> °C	$I_p$ , eV	$\mu_0$ , cm <sup>2</sup> /V·s ( $E = 0$ V/cm)
9,9'-Spirobifluorene-based materials					
	Spiro-OMeTAD <sup>[2]</sup>	124 ( $T_m=245$ °C) <sup>c</sup>	449	5.0	$4.1 \cdot 10^{-5}$
	<b>V1240</b>	168	437	5.28	$5.6 \cdot 10^{-6}$ [d]
	<b>V1267</b>	138	512	4.9	$3.6 \cdot 10^{-4}$ [d]
Fluorene-based materials with methoxyphenyl and carbazolyl chromophores					
	<b>V1222</b>	147	452	4.93	$3.9 \cdot 10^{-4}$ [d]
	<b>V1226</b>	132	440	4.95	$2.7 \cdot 10^{-3}$
	<b>V1238</b>	76	401	5.02	$2.9 \cdot 10^{-5}$
Fluorene-based materials with carbazolyl chromophores					
	<b>V1257</b>	196	490	4.85	$3.6 \cdot 10^{-5}$ [d]
	<b>V1258</b>	183	460	4.85	$1.2 \cdot 10^{-5}$ [d]
	<b>V1269</b>	126	514	4.96	$3 \cdot 10^{-5}$ [d]

<sup>a</sup> Glass transition temperature, determined in the second DSC heating cycle; <sup>b</sup> Decomposition temperature, corresponding to the 5% weight loss; <sup>c</sup> Melting point was not detected for the new compounds; <sup>d</sup> Values of the hole drift mobility were evaluated by extrapolation of the results, obtained from the measurements of the mixture of the HTMs with polymeric PC-Z matrix.

To evaluate the thermal behaviour of new HTMs, thermogravimetric analysis (TGA) and differential scanning calorimetry (DSC) measurements were performed. Table 3.1 reveals the parameters of the newly synthesized compounds, as well as that of the reference material Spiro-OMeTAD. Overall, all new materials are stable up to 400 °C, which is well above operating temperatures of the solar cells.

For the compounds containing fluorene core and two carbazolyl moieties the  $T_{dec}$  values are in the range of 402-454 °C, with the lower value observed for the material **V1238**



The PerTPV project has received funding from the European Union's Horizon 2020 research and innovation programme under grant agreement No 763977.

with the longest aliphatic chain. HTMs with the four carbazolyl fragments in general have shown higher  $T_{\text{dec}}$  values in the range of 461-515 °C.

The glass transition temperatures ( $T_g$ ) for all new compounds are given in Table 3.1. New spirobifluorene class compounds **V1240** and **V1267** have shown higher  $T_g$  than Spiro-OMeTAD. The  $T_g$  of new fluorene derivatives with methoxyphenyl fragments (**V1222**, **V1226**, **V1238**) decreases with the lengthening of the alkyl chain and is the lowest for the material **V1238** with an ethylhexyl substituent in the central fluorene moiety. Analysing the DSC results of the second group of compounds with four carbazolyl moieties (**V1257**, **V1258**, **V1269**), similar trend in  $T_g$  was observed. Comparing the first (**V1222**, **V1226**, **V1238**) and second (**V1257**, **V1258**, **V1269**) groups of compounds with each other, it was observed that the additional carbazolyl moieties increases the glass transition temperature by around 50 °C up to 196 °C. It is important to note, that melting of the crystals was not observed for any of the new materials, indicating that they have only an amorphous state, which is advantageous for the formation of the homogenous films.

To evaluate energy levels of the new compounds solid-state ionization potential ( $I_p$ ) values were measured by means of photoelectron spectroscopy in air (PESA) technique (Table 3.1). Fluorene derivatives with two carbazolyl moieties (**V1222**, **V1226**, **V1238**) demonstrate ionization potentials in the range of 4.9-5.0 eV. Two additional carbazolyl moieties in derivatives (**V1257**, **V1258**, **V1269**) result in further decrease in  $I_p$  to 4.8-4.9 eV. The ionization potentials of spirobifluorene derivatives **V1240** and **V1267** follows the same trend, additional carbazole fragments reduce ionization potential from 5.26 to 4.9 eV, overall investigated materials demonstrate energy levels suitable for the use narrow bandgap perovskite absorbers.

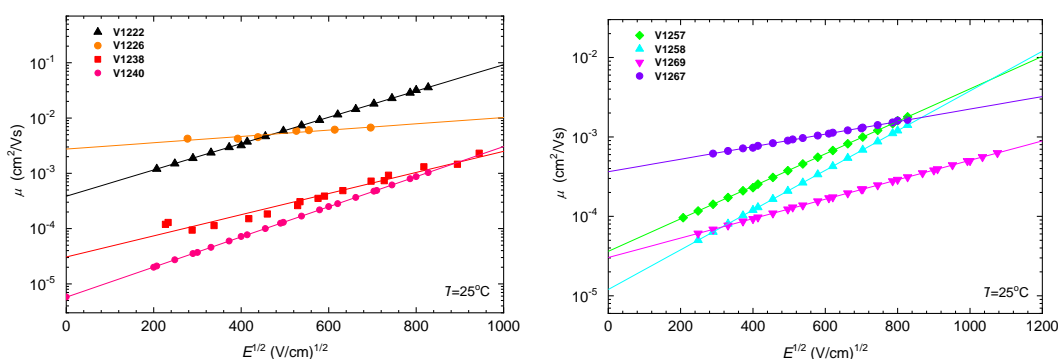


Figure 3.3. Electric field dependencies of the hole drift mobilities of investigated HTMs.

Xerographic time-of-flight (XTOF) method (Figure 3.3, Table 3.1) was used to measure the carrier drift mobility of the investigated materials. Overall investigated HTMs display one order of magnitude higher hole mobility than Spiro-OMeTAD, with **V1226** demonstrating best result of  $2.7 \times 10^{-3} \text{ cm}^2 \text{V}^{-1} \text{s}^{-1}$ . Despite many similarities between the molecules, the differences in carrier drift mobility could be explained by the neater spatial configuration and consequentially smaller charge hopping distances.

Preliminary investigation of the doped HTMs in the perovskite devices (FTO/c-TiO<sub>2</sub>/m-TiO<sub>2</sub>/SnO<sub>2</sub>/triple cation perovskite/HTM/Au) revealed that compounds containing more carbazolyl units perform better (PCE in the range of 17-18.4%) and are more promising for further studies than those with fewer carbazolyl units (PCE in the range of 13-16%). Interestingly, the best results were obtained with the most branched derivative **V1267** (PCE= 18.39%).

### 3.1.2 Carbazole-based enamines

New carbazole-based enamines, **MeO5PECz** and **MeO4PEBCz** have been obtained in facile one-step synthesis without the use of expensive organometallic catalysis or costly



The PerTPV project has received funding from the European Union's Horizon 2020 research and innovation programme under grant agreement No 763977.

purification techniques, resulting in significantly reduced cost compared with most other HTMs used in PSCs. Furthermore, no chemical oxidation is required to reach high PCEs, making these materials attractive alternatives for applications in PSCs. One-step synthesis of enamines **MeO5PECz** and **MeO4PEBCz** from commercially available carbazole diamines can be seen in Figure 3.4.

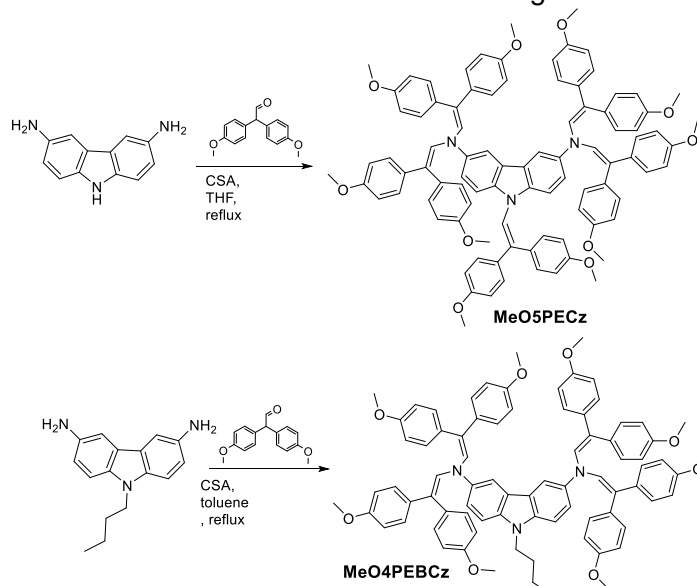


Figure 3.4. Synthesis of carbazole enamines **MeO5PECz** and **MeO4PEBCz**.

Carbazole derivatives **MeO5PECz** and **MeO4PEBCz** have been obtained without the use of expensive palladium-catalyzed cross-coupling in a simple acid-catalyzed condensation reaction between respective carbazole diamines and bis(4-methoxyphenyl)-acetaldehyde (Figure 3.4). Afterwards, **MeO5PECz** and **MeO4PEBCz** were purified by recrystallization, without the need for expensive and time-consuming column chromatography.

The thermal stability of the HTMs was determined using thermogravimetric analysis, the results are shown in Figure 3.5 and Table 3.2. The tested materials demonstrated 5% weight loss just slightly below 400 °C, proving that they are sufficiently thermally stable for application in PSCs. Furthermore, the rapid weight loss seen in Figure 3.5 suggests that the investigated materials can readily evaporate and demonstrate potential for vacuum deposition.

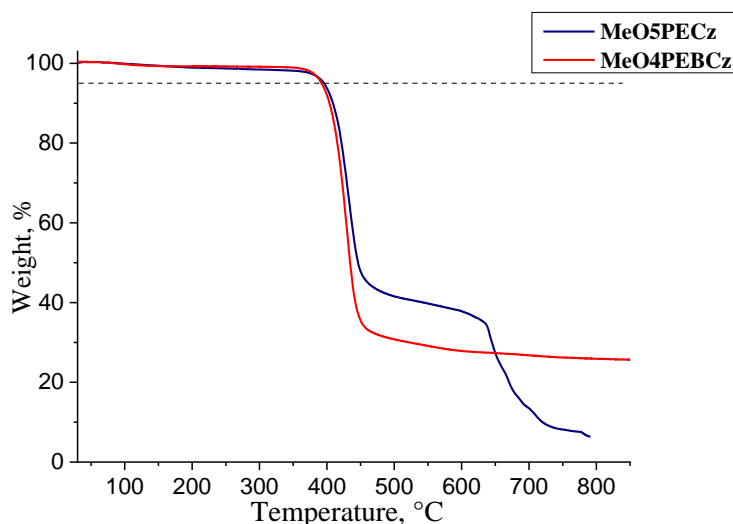


Figure 3.5. TGA heating curves of **MeO5PECz** and **MeO4PEBCz**.



The PerTPV project has received funding from the European Union's Horizon 2020 research and innovation programme under grant agreement No 763977.

Under working conditions, PSCs can reach temperatures well above 65 °C; therefore, HTMs must demonstrate high glass transition temperatures.  $T_g$  of the enamines was measured using differential scanning calorimetry (DSC), and the results showed that both **MeO5PECz** and **MeO4PEBCz** have relatively high  $T_g$ , 152 °C and 140 °C respectively (Table 3.2).

Table 3.2. Thermal characteristics of the new HTMs and spiro-OMeTAD for comparison.

Compound	$T_g^{(a)}$ , °C	$T_m^{(b)}$ , °C	$T_{dec}^{(c)}$ , °C
MeO5PECz	152	204	395
MeO4PEBCz	140	261	392
Spiro-OMeTAD	124	245	449

<sup>a</sup> Determined by DSC: scan rate = 10 °C min<sup>-1</sup>, N<sub>2</sub> atmosphere; second run; <sup>b</sup> Determined by DSC: scan rate = 10 °C min<sup>-1</sup>, N<sub>2</sub> atmosphere; first run; <sup>c</sup> Onset of decomposition determined by TGA: heating rate = 10 °C min<sup>-1</sup>, N<sub>2</sub> atmosphere.

The difference in  $T_g$  becomes clearer when we look at the structure of the HTMs. Both organic semiconductors are carbazole derivatives, however, **MeO5PECz** has an additional bis(4-methoxyphenyl)ethenyl fragment at the 9-position of the carbazole moiety, while **MeO4PEBCz** has an aliphatic butyl chain instead, which reduces the bulkiness of the molecule thus lowering the  $T_g$ .

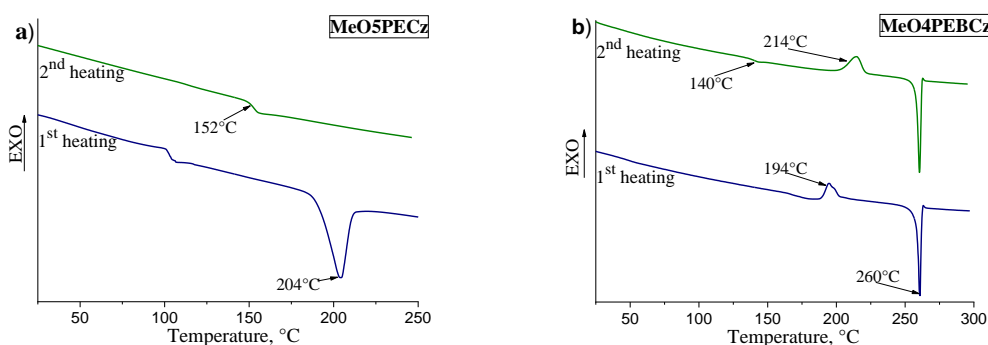


Figure 3.6. DSC heating curves of a) **MeO5PECz** and b) **MeO4PEBCz** (heating and cooling rate 10 K min<sup>-1</sup>).

Furthermore, both materials are partially crystalline with melting temperatures of 204°C for **MeO5PECz** and 261°C for **MeO4PEBCz** (Figure 3.6). Interestingly, during the second heating of **MeO5PECz**, no crystallization takes place, which is important for the formation of good quality thin films, since spontaneous and uncontrollable crystallization causes charge trapping and layer separation which results in a drop of device efficiency. While **MeO4PEBCz** starts to crystallize during first and second heating, none the less it also possesses relatively high  $T_g$  which, should lower the probability of the crystallization occurring in a working device quite significantly.



Table 3.3. Photophysical properties of the synthesized materials and Spiro-OMeTAD for comparison.

Compound	$I_p$ , eV <sup>(a)</sup>	$\mu_0$ , cm <sup>2</sup> V <sup>-1</sup> s <sup>-1</sup> <sup>(b)</sup>	$\mu$ , cm <sup>2</sup> V <sup>-1</sup> s <sup>-1</sup> <sup>(c)</sup>
<b>MeO5PECz</b>	5.01	$3.7 \times 10^{-5}$	$7.8 \times 10^{-4}$
<b>MeO4PEBCz</b>	4.96	$1.2 \times 10^{-4}$	$1.1 \times 10^{-3}$
Spiro-OMeTAD	5.00	$4.1 \times 10^{-5}$	$5 \times 10^{-4}$

<sup>a</sup> Ionization potential was measured by photoemission spectroscopy in air from films; <sup>b</sup> Hole mobility value at zero field strength; <sup>c</sup> Hole mobility value at the electric field strength of  $6.4 \times 10^5$  Vcm<sup>-1</sup>.

Photoemission spectroscopy in air was used to measure the ionization potential of the investigated carbazole derivatives in the solid-state (the error of this method is evaluated as  $\pm 0.03$  eV). Both materials have similar  $I_p$  of  $\sim 5.00$  eV (Table 3.3); interestingly, additional electron donating bis(4-methoxyphenyl)ethenyl moiety in **MeO5PECz** has a negligible effect on energy levels, compared with **MeO4PEBCz**,  $I_p$  even increases slightly. Steric hindrance resulting from five bis(4-methoxyphenyl)ethenyl fragments connected to the carbazole core could be the main factor behind it.

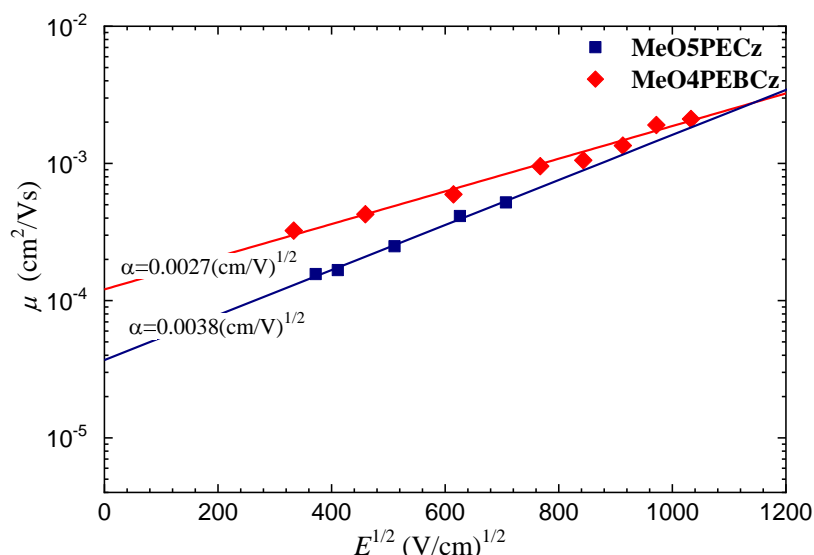


Figure 3.7. Carrier Drift mobility of the tested HTMs.

Xerographic time-of-flight (XTOF) method (Figure 3.7) was used to measure the drift carrier mobility of the investigated materials. **MeO4PEBCz** displayed slightly higher mobility of  $1.1 \times 10^{-3}$  cm<sup>2</sup>V<sup>-1</sup>s<sup>-1</sup> versus  $7.8 \times 10^{-4}$  cm<sup>2</sup>V<sup>-1</sup>s<sup>-1</sup> for **MeO5PECz** (Table 3.3). Despite many similarities between the molecules, the difference in drift carrier mobility could be explained by the neater spatial configuration of **MeO4PEBCz** and consequentially smaller charge hopping distance. This correlates well with the  $I_p$  results, as additional electron donating bis(4-methoxyphenyl)ethenyl moiety in **MeO5PECz** increases steric hindrance in the molecule.

These new carbazole based HTMs were tested in perovskite solar cells (FTO/SnO<sub>2</sub>/FA<sub>0.83</sub>Cs<sub>0.17</sub>Pb(I<sub>0.9</sub>Br<sub>0.1</sub>)<sub>3</sub>/HTM/Au) The new HTMs in dopant free setup, demonstrated PCE in the range between 16.5% and 17%, interestingly doped HTMs showed very similar performance in the range between 17% and 17.5%.



The PerTPV project has received funding from the European Union's Horizon 2020 research and innovation programme under grant agreement No 763977.

## 3.2. Deep HOMO hole transporting materials (KTU)

### 3.2.1 Spirofluorene-based enamines

Similarly, as with shallow HOMO materials, we have investigated spirobifluorene-based derivatives in the HTMs with significantly deeper HOMO energy levels. Several groups studied central 9,9'-spirobifluorene-linked HTMs including dimethylfluorenyl-, ethylcarbazoyl-, and fluorinated methoxyphenyl-terminated examples. Generally, such spiro-centred HTMs are designed by linking prebrominated spiro core species with costly diphenylamine or borylated triphenylamine both containing methoxy-substituted side groups using C–N or C–C cross-coupling chemistry, respectively. Such coupling reactions require stringent reaction conditions resulting in several disadvantages including inert reaction conditions, expensive transition metal catalysts and time-consuming purification procedures due to the inherent formation of side products for this type of reactions. Moreover, residues of metal catalyst may remain in the hole transporting layer that act as traps, deteriorating charge-transporting properties and negatively affecting the performance of the resulting devices. In this sense, enamine condensation chemistry has several advantages being an excellent perspective moving away from palladium-catalysed reactions since water is the only side-product and expensive catalysts are not required, as schematically compared in Figure 3.10. Moreover, simple product workup and purification may significantly reduce the cost of the final product.

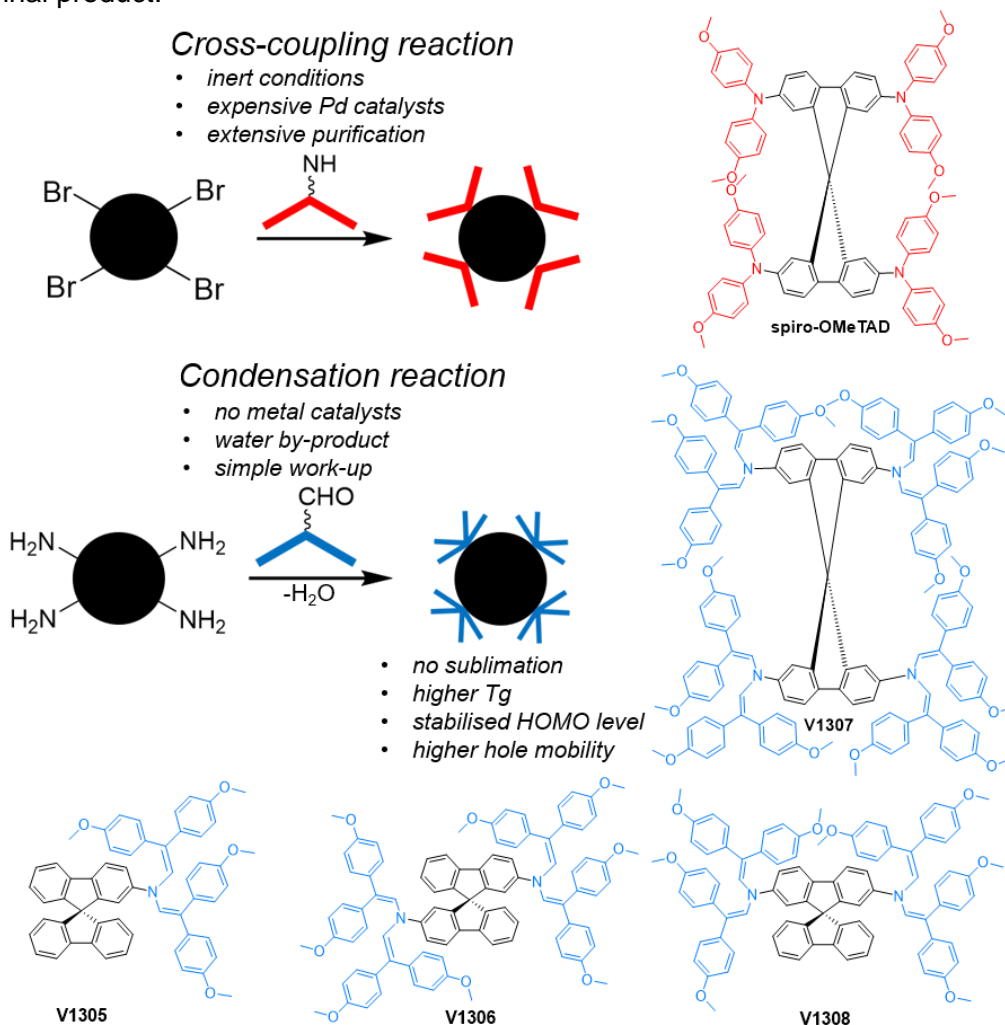


Figure 3.10. Schematic comparing of cross-coupling and condensation reactions for the synthesis of spiro-OMeTAD and novel enamine HTMs.





Figure 3.10 presents the chemical structures of the parent spiro-OMeTAD and enamine-based analogs (**V1307**, **V1305**, **V1306** and **V1308**). Four HTMs containing well-established spirobifluorene core with introduced enamine arms were synthesized simply by condensing aminated-precursors with 2,2-bis(4-methoxyphenyl)acetaldehyde. The condensation reaction was performed under ambient conditions and water is the only by-product, continuously separated using a Dean–Stark trap that accelerates the formation of the final product.

Thermogravimetric analysis suggests that novel HTMs start decomposing at around 400 °C (Table 3.5), which is far above the temperature for conventional device operation. Differential scanning calorimetry measurements indicate that **V1305**, **V1306** and **V1308** could exist in both crystalline and amorphous states similarly as spiro-OMeTAD. Interestingly, **V1307** is fully amorphous and has the highest glass transition temperature ( $T_g$ ) of 169 °C, which should result in improved quality of the **V1307** layers. We also note that all synthesized HTMs have higher  $T_g$  than spiro-OMeTAD (124 °C) meaning that the introduction of enamine fragments improves the morphological stability.

The solid-state ionization potential ( $I_p$ ) of **V1305**, **V1306**, **V1307** and **V1308** was determined using electron photoemission spectroscopy in air (PESA) of the thin films to assess the HOMO energy level of spiro-enamine HTMs (Table 3.5).  $I_p$  values of **V1305**, **V1306**, **V1307** and **V1308** were found to be 5.33, 5.37, 5.46, and 5.46 eV, respectively, which is significantly stabilised comparing to that of spiro-OMeTAD (5.00 eV).

Xerographic time of flight (XTOF) measurements were used to determine the charge mobility of the V-series layers. Dependences of hole drift mobility on electric field strength are shown in Figure 3.11. **V1308** and **V1307** exhibited the highest zero-field hole drift mobility ( $\mu_0$ ) among the series having the values of  $9.4 \times 10^{-4}$  and  $6.4 \times 10^{-4}$  cm<sup>2</sup>/Vs, respectively, both outperforming that of spiro-OMeTAD ( $\mu_0 = 1.3 \times 10^{-4}$  cm<sup>2</sup>/Vs). The thermal, optical, and photoelectrical properties of the spiro-enamines are summarized in Table 3.5.

Table 3.5. Thermal, optical and photophysical properties of newly synthesized enamines.

Compound	$T_m$ , °C <sup>a)</sup>	$T_c$ , °C <sup>a)</sup>	$T_g$ , °C <sup>a)</sup>	$T_{dec}$ , °C <sup>a)</sup>	$I_p$ , eV <sup>c)</sup>	$\mu_0$ , cm <sup>2</sup> V <sup>-1</sup> s <sup>-1</sup> <sup>f)</sup>
<b>V1305</b>	243	-	131	380	5.33	$1.7 \cdot 10^{-5}$
<b>V1306</b>	294	226	154	402	5.37	$5.4 \cdot 10^{-6}$
<b>V1307</b>	-	-	169	401	5.46	$6.4 \cdot 10^{-4}$
<b>V1308</b>	305	203	158	371	5.46	$9.4 \cdot 10^{-4}$

<sup>a)</sup>Melting ( $T_m$ ), crystallization ( $T_c$ ), glass transition ( $T_g$ ) and decomposition ( $T_{dec}$ ) temperatures observed from DSC and TGA, respectively (10 °C/min, N<sub>2</sub> atmosphere); <sup>b)</sup>Ionization energies of the films measured using PESA; <sup>f)</sup>Mobility value at zero field strength.



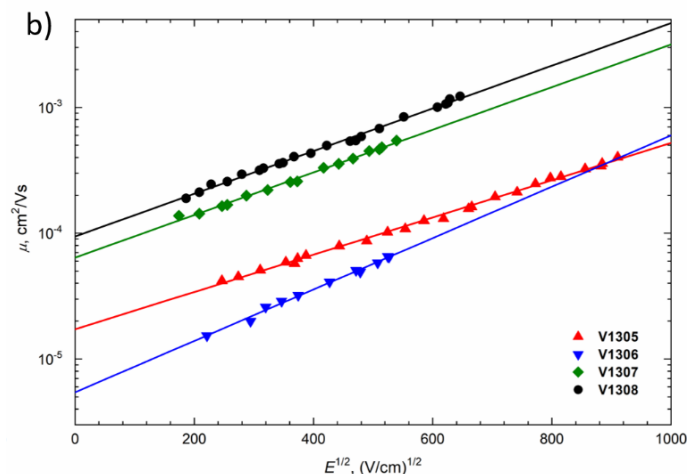


Figure 3.11. Electric field dependencies of the hole-drift mobility in spiro-enamines.

Investigation in *n-i-p* solar cells was carried out with the device layout FTO/c-TiO<sub>2</sub>/m-TiO<sub>2</sub>/SnO<sub>2</sub>/perovskite/HTM/Au. The perovskite composition used was the triple cation perovskite [(FAPbI<sub>3</sub>)<sub>0.87</sub>(MAPbBr<sub>3</sub>)<sub>0.13</sub>]<sub>0.92</sub>(CsPbI<sub>3</sub>)<sub>0.08</sub> and the HTM is doped with the bis-(trifluoromethylsulfonyl)imide lithium salt (LiTFSI) and cobalt(III)-tris(bis-(trifluoromethylsulfonyl)imide) (CoTFSI), *tert*-butylpyridine (TBP) was also added to the HTM solution to improve the HTM morphology and increase the LiTFSI solubility. The most efficient devices containing **V1305**, **V1307** and **V1308** have similar power conversion efficiency (PCE) values of 19.0, 19.2 and 19.1%, respectively.

The impact of differently substituted central spirobifluorene core going from single- to multi-armed enamines was evaluated, showing that a higher degree of substitution has several advantages. First, the perpendicular arrangement of the two overcrowded enamine-based molecular halves leads to a high steric demand of the resulting rigid structure, efficiently suppressing molecular interactions. Furthermore, compound **V1307** with a larger globular structure, higher molecular weight, and small intermolecular cohesion result in a high stability of the amorphous state. Comparing directly the dimethoxydiphenylamine and bisdimethoxydiphenylamine donating fragments of spiro-OMeTAD and **V1307**, respectively, the latter has some merits. First, bisdimethoxydiphenylamine being a less strong donor results in the stabilized HOMO values. Second, more pronounced and higher degree of conjugation in enamine arms results the better charge transport through **V1307** denser packed layer. These advantages were found to enable novel enamine-derived spirobifluorene HTMs for successful application in PSCs reaching a photovoltaic performance of up to 19.2% with excellent long-term stability. With this we demonstrate the simple enamine condensation chemistry as a universal approach to obtain highly efficient and stable HTMs.

### 3.2.3 Tröger's base derivative containing larger diphenylbenzidine units

Continuing with the investigation of the Tröger's base core reported in the deliverable D1.6, larger conjugated moiety *N,N*-bis(3-methylphenyl)-*N,N*-diphenylbenzidine (TPD) was introduced into the system.

TPD is known to have hole drift mobility as high as  $1.1 \times 10^{-3} \text{ cm}^2 \text{ V}^{-1} \text{ s}^{-1}$ , but unfortunately it lacks thermal and morphological stability and tends to crystallize readily. This limitation is also noticeable in Spiro-OMeTAD and could potentially be overcome by finding an alternative to spiro carbon as the connecting and orienting core, and conjoining TPD-type moieties in a different fashion. Tröger's base (TB) can serve this role as a functional core, allowing the synthesis of HTMs with decent properties and high charge mobility. The V-shaped structure of TB provides an angle orientation for the conjugated  $\pi$ -systems attached to it and the rigidity of the TB scaffold (as the high molecular mass via



its 2-fold functionalization) impairs crystallization, making the TB derivatives highly amorphous and endowing them with significantly increased glass transition temperatures.

**V1160** was synthesized in a straightforward way starting from the commercially available precursors. The final compound was obtained in high yield utilizing Buchwald-Hartwig amination conditions (Figure 3.12). After purification, V1160 was isolated as a slightly coloured, amorphous powder, soluble in common organic solvents (e.g. THF, toluene,  $\text{CHCl}_3$ ).

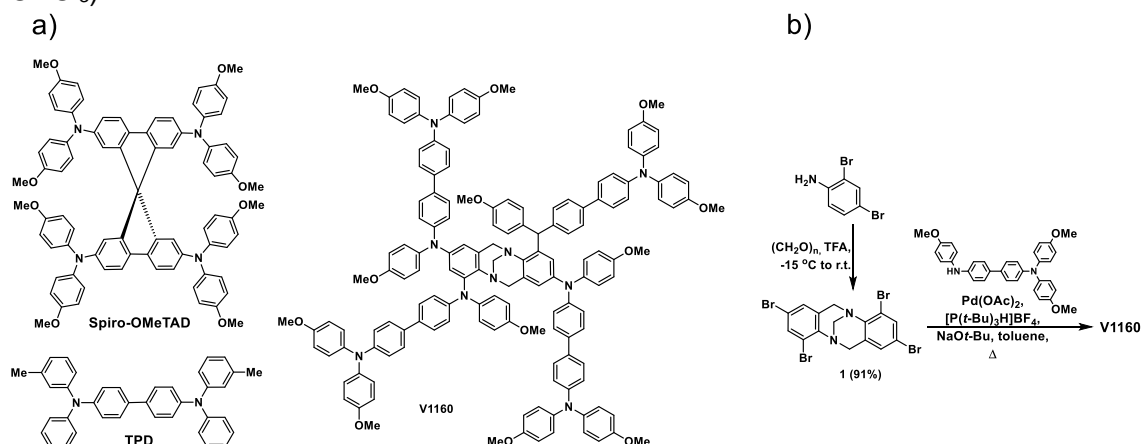


Figure 3.12. (a) Molecular structures of the Spiro-OMeTAD, TPD, and the new HTM **V1160**; (b) Synthesis of the **V1160**.

It is very beneficial to obtain fully amorphous HTM film as it improves morphological stability of the HTM layer. Therefore, differential scanning calorimetry was used to study the phase transitions of the **V1160**. During the first heating cycle ( $10 \text{ K min}^{-1}$ ) no melting transition was detected, and only a glass transition can be observed (Figure 3.13a). During the cooling stage, no crystallization occurred and on the second heating scan, a  $T_g$  at  $166^\circ\text{C}$  was observed, which is significantly higher than that of Spiro-OMeTAD ( $124^\circ\text{C}$ ). The absence of a crystalline phase for **V1160** makes this material an attractive candidate for the stable PSC fabrication, as device failure due to the crystallization of HTM is mitigated. In addition, the thermal stability of **V1160** was evaluated by thermogravimetric analysis to reveal that material is stable up to  $420^\circ\text{C}$ , which is more than sufficient for practical applications in optoelectronic devices.

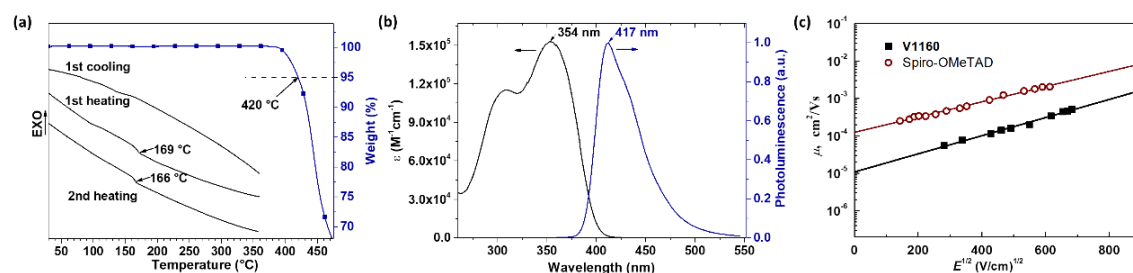


Figure 3.13. (a) DSC (black lines) and TGA (blue line) analysis of **V1160**; (b) UV/vis absorption (black line) and normalized PL (blue line) spectra of **V1160** in THF; (c) hole-drift mobility measurements of **V1160** and Spiro-OMeTAD.

To investigate the position of the energy levels of **V1160**, photoelectron spectroscopy in air (PESA) of the HTM film was performed. The solid-state ionization potential value ( $I_p$ ) was measured as  $5.24 \text{ eV}$ . The ability of **V1160** to transport holes was evaluated by measuring xerographic time-of-flight (XTOF) hole drift mobilities. As can be seen from Figure 3.13c, for **V1160**, the hole drift mobility is  $1.1 \times 10^{-5} \text{ cm}^2 \text{ V}^{-1} \text{ s}^{-1}$  at low electrical fields ( $\mu_0$ ). Despite having a high amount of TPD-type moieties fused in the TB core,



The PerTPV project has received funding from the European Union's Horizon 2020 research and innovation programme under grant agreement No 763977.

**V1160** demonstrated lower  $\mu_0$  value than Spiro-OMeTAD. Such behaviour can be attributed to the higher disorder in the molecular structure due to the bulky nature of the molecule, interfering with the favourable arrangement with adjacent molecules. Investigation in *n-i-p* solar cells was carried out with the device layout FTO/ compact TiO<sub>2</sub>/ mesoporous TiO<sub>2</sub>/ amorphous SnO<sub>2</sub>/ [(FAPbI<sub>3</sub>)<sub>0.87</sub>(MAPbBr<sub>3</sub>)<sub>0.13</sub>]<sub>0.92</sub>(CsPbI<sub>3</sub>)<sub>0.08</sub>/ HTM/ Au. **V1160** was investigated both with and without dopants. PSCs with doped **V1160** as HTM showed maximum PCE of 18.3% which is comparable with that of the reference Spiro-OMeTAD-based PSCs (19.2%), obtained in the same series of batches. In addition, **V1160** was tested in a dopant-free configuration. Devices with dopant-free **V1160** resulted in a moderate PCE of 12.6%.

### 3.3. Hole transporting materials capable of forming self-assembled monolayers (KTU)

In the scope of future high-throughput commercialization, it is crucial to keep the simplicity and robustness that PSCs exhibit. Additionally, it is desirable to minimize parasitic absorption and to use low-cost materials that are suitable for a variety of substrates with arbitrary surfaces and large areas, in order to expand the applicability fields of PSCs. These ambitions could be realized by using self-assembled monolayers (SAMs) as charge-selective contacts. The required material quantities are minimal; the substrate compatibility is manifold and process control is simple, with the molecules autonomously forming a functional layer in a self-limiting process by design. These molecules covalently bind to the transparent conductive oxide (TCO), e.g. indium tin oxide (ITO), on which the perovskite absorber crystallizes. Due to their hole-selectivity, the SAMs can replace the classical hole-transporting layer.

The SAMs act as simple hole-selective contacts that can be prepared by classical dip-coating or spin-coating within wide processing windows. As reported earlier in deliverable D1.6, maximum PCE of over 21%, which is comparable to current record-efficiencies in the p-i-n architecture can be achieved using SAMs **2PACz** and **MeO-2PACz**. Notably, this PCE is achieved without any perovskite post-treatments, additives, dopants or interlayers that are usually used for high PCEs after delicate fine-tuning. In addition, investigated SAMs work efficiently with both solution and vacuum deposited perovskite compositions, assuring that hole-extraction by SAMs is a universal approach.

The presence of SAM HTMs on the surface of the ITO was confirmed by FTIR, VSFG, contact angle, and  $I_p$  measurements. Ionization potential measurements demonstrated that  $I_p$  of the synthesized SAMs covers a wide range of energy levels (**MeO-2PACz**  $I_p$ =5.2 eV, **Me-4PACz**  $I_p$ =5.45 eV, **2PACz**  $I_p$ =5.7 eV).

In summary, we demonstrate that solar cells can be fabricated without additional passivation layers, additives or dopants. Together with the minimal material consumption, manifold substrate compatibility and simplicity during fabrication, the SAM contacts might present a realistic way to further progress perovskite photovoltaics into a low-cost, wide-spread technology. Very encouraging SAM results obtained with perovskite/silicon tandem initial testing platform as well as results in single junction perovskite solar cells allow us to be optimistic that self-assembled monolayer approach will be beneficial for the perovskite/perovskite tandem devices as well.

## 4. Conclusions

### 4.1. Perovskite absorbers

One of the important objectives for the development of tandem devices was development of compatible wide and narrow bandgap perovskite absorbers. The aim for the low bandgap perovskite was 1.2 to 1.3 eV, the target bandgap for the wide bandgap perovskite is 1.7 to 1.8 eV as identified in D1.1.



The PerTPV project has received funding from the European Union's Horizon 2020 research and innovation programme under grant agreement No 763977.

PERTPV is aiming to prepare perovskite solar cells, using processes that are compatible with industrial methods for large volume manufacturing. In particular, solution-based slot die-coating and printing methods in parallel to vacuum sublimation. Therefore, perovskite absorber compositions were developed in two directions to suite requirements of solution processing and vacuum deposition.

#### 4.1.1 Solution processed wide bandgap perovskite absorbers

Great progress on efficiency and stability by doping with a piperidinium salt. The composition of choice is  $\text{FA}_{0.75}\text{Cs}_{0.25}\text{Pb}(\text{I}_{0.6}\text{Br}_{0.4})_3$ , with efficiency over 16%.

#### 4.1.2 Solution processed narrow bandgap perovskite absorbers

From the tested narrow bandgap perovskite absorbers suitable for solution based processes Pb:Sn mixed metal perovskite compositions  $(\text{FA}_{0.83}\text{Cs}_{0.17})(\text{Pb}_{0.7}\text{Sn}_{0.3})\text{I}_3$  (1.33 eV) and  $(\text{FA}_{0.83}\text{Cs}_{0.17})(\text{Pb}_{0.5}\text{Sn}_{0.5})\text{I}_3$  (1.3 eV) show the greatest promise. Demonstrating power conversion efficiency values of 17.6 and 18.1 % accordingly.

#### 4.1.3 Vacuum deposited wide bandgap perovskite absorbers

From the tested wide bandgap perovskite absorbers suitable for vacuum deposition processes, perovskite compositions  $\text{FA}_{0.65}\text{Cs}_{0.35}\text{Pb}(\text{I}_{0.73}\text{Br}_{0.27})_3$  (1.75 eV) and  $\text{FA}_{0.61}\text{Cs}_{0.39}\text{Pb}(\text{I}_{0.70}\text{Br}_{0.30})_3$  (1.77 eV) show the greatest promise. The best PSC obtained with the wide-bandgap perovskite with  $E_g = 1.75$  eV demonstrated maximum PCE exceeding 16.5%, while highest bromide content perovskite absorbers ( $E_g = 1.77$  eV), reached a PCE of 15.6 %.

#### 4.1.4 Vacuum deposited narrow bandgap perovskite absorbers

From the tested narrow bandgap perovskite absorbers suitable for vacuum deposition processes, perovskite composition  $\text{MACsSnPbI}_3$  (1.3 eV) shows the greatest promise, the optimum performance is obtained for the  $\text{SnPbMACs}$  perovskite with a  $\text{SnPb}$  to  $\text{MACs}$  ratio of 2.3:1.

## 4.2. Charge transporting materials

In order for these perovskite absorbers to function effectively, development of efficient charge extracting materials is essential. As with perovskite absorbers discussed earlier, development of aforementioned charge transporting materials has to be conducted in two directions: solution processable and thermally sublimable compounds.

#### 4.2.1 Electron transporting materials

Due to various structure and synthesis related reasons development of electron transporting materials is more problematic and selection of such compounds is more limited, compared with hole transporting analogues. In this project we looked at some of the main groups of materials that could be applied as ETMs in perovskite solar cells, unfortunately, their performance was too low, indicating that further work needs to be done in this area. At the moment, the best choice for the n-i-p architecture PSC remains  $\text{SnO}_2$  and for p-i-n architecture  $\text{C}_{60}$ .



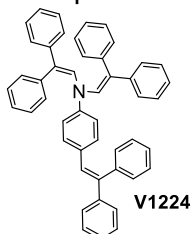
*The PerTPV project has received funding from the European Union's Horizon 2020 research and innovation programme under grant agreement No 763977.*

#### 4.2.2 Hole transporting materials

For perovskite absorbers to function effectively, energy levels of hole extracting materials should match the energy levels of the wide and low bandgap perovskite absorbers. Ionisation potential of the developed HTMs ideally should be in the range between 5.2 and 5.7 eV for wide bandgap absorbers, and 4.8 to 5.1 eV for narrow bandgap absorbers.

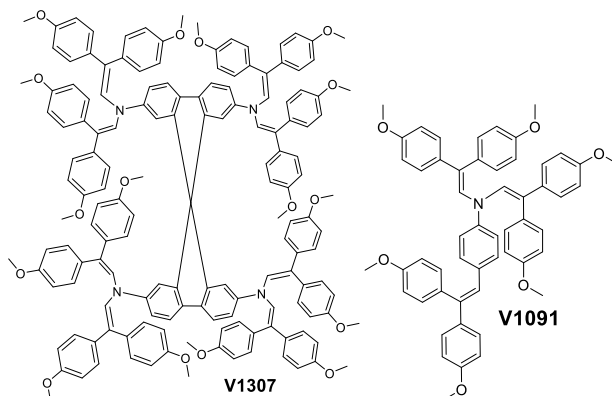
##### Vacuum deposited hole transporting materials

Among new HTMs, suitable for vapor deposition, **V1224** ( $I_p$ = 5.3 eV) shows the greatest promise. Devices using this enamine compound demonstrated PCE of 18.4%.

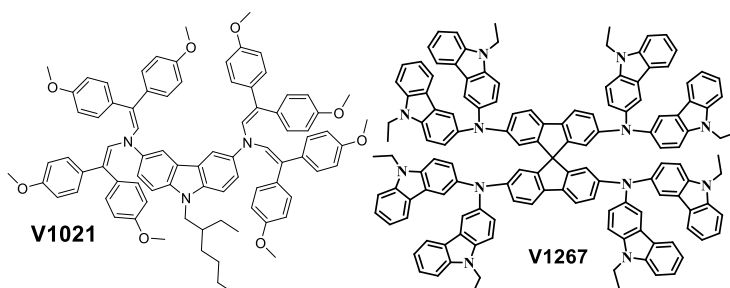


##### Solution processed hole transporting materials

For wide bandgap perovskite absorbers with n-i-p device architecture, bifluorene-based enamine **V1307** ( $I_p$ = 5.46 eV) and aniline-based enamine **V1091** ( $I_p$ = 5.2 eV) show most promise. Perovskite solar cells utilising these enamine derivatives have demonstrated 19.2 % and 20.2 % accordingly.



Carbazole enamine **V1021** ( $I_p$ = 4.93 eV) and bifluorene-based derivative **V1267** ( $I_p$ = 4.9 eV) are the most promising HTM for narrow bandgap perovskite absorbers with n-i-p device architecture, demonstrating PCE of 19 % and 18.4 % accordingly.

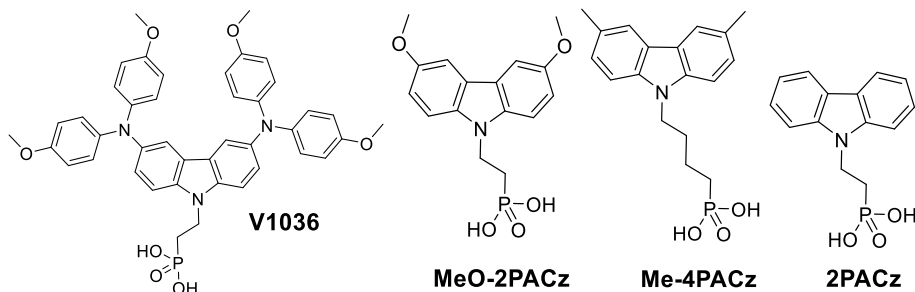


Finally, for solution processed p-i-n type perovskite solar cells hole transporting materials capable of forming self-assembled monolayers are the most suitable choice. Ionization





potential measurements demonstrated that  $I_p$  of the synthesized SAMs covers a wide range of energy levels (**V1036**  $I_p=5.0$  eV, **MeO-2PACz**  $I_p=5.2$  eV, **Me-4PACz**  $I_p=5.45$  eV, **2PACz**  $I_p=5.7$  eV) and they are suitable for both wide as well as narrow bandgap perovskite absorbers. Devices with SAM HTMs have consistently demonstrated PCE close to 21 %, these materials have also been shown to function efficiently in other tandem devices. Furthermore, they have been commercialized by two chemical companies, Dyenamo (Sweden) and TCI (Japan) and are among the most promising hole transporting materials developed during course of this project.



The PerTPV project has received funding from the European Union's Horizon 2020 research and innovation programme under grant agreement No 763977.